Steady Flow Simulation of a Polymer-Diluent Solution Through an Abrupt Axisymmetric Contraction Using Internally Consistent Rheological Scaling

Shunahshep Shukla, Kurt W. Koelling

Chemical and Biomolecular Engineering, The Ohio State University, Columbus, Ohio

Received 29 January 2006; accepted 17 November 2006
DOI 10.1002/app.26664
Published online 8 July 2007 in Wiley InterScience (www.interscience.wiley.com).

ABSTRACT: In this work, a new methodology is developed that describes the viscoelastic scaling of a polymer-physical foaming agent (PFA) solution in a detailed and internally consistent manner. The approach is new in that while previous researchers have largely focused on scaling down experimentally obtained high pressure polymer-PFA solution viscosity data onto a master curve for the viscosity of the undiluted polymer melt at a reference temperature and atmospheric pressure, we have generated the shear viscosity data required for our simulations by systematically scaling up the viscosity values obtained from measurements on a pure polymer melt to the desired temperature, pressure, and concentration values characterizing the flow. Simulations have been run for the flow of a polymer-PFA solution through an extrusion foaming die with an abrupt axisymmetric contraction and good qualitative agreement is obtained with experimental pressure drop measurements obtained previously in our laboratory. The pressure drop rates and temperature rise rates have been estimated at the surface of incipient nucleation. Because of the short residence times in the die for the microcellular foaming process, approximating the flow through the die as a single phase flow in our simulations still gives useful insights into the dynamics of the flow. © 2007 Wiley Periodicals, Inc. J Appl Polym Sci 106: 1053–1074, 2007

Key words: polystyrene; polymer processing; supercritical fluids; microcellular foaming; flow modeling

INTRODUCTION

US consumption of plastic foams was projected to exceed 7.8 billion pounds in 2005.[1] Thermoset polyurethane, polystyrene (PS), and polyethylene (PE) foams dominate the plastics foam market with PS foams accounting for 25% of the total market share.[2] PS foams produced by continuous processes like extrusion or semibatch processes like injection molding represent 90% of the total PS foam production in the United States.

Low-density thermoplastic foams have been produced in the plastics industry for over four decades now. Because of the commercial importance and complexity of the polymer foaming process, numerous studies have been carried out to understand the effect of the processing variables on the final foam morphology. Initial studies focused more on thermoplastic foam extrusion using chemical blowing agents since foam production using chemical blowing agents is easier than foam production using physical blowing agents. Notable among the studies on continuous foaming of polymers using chemical blowing agents are the studies conducted by Hansen,[3] Han et al.,[4] Blyler and Kwei,[5] and Oyanagi and White[6] on the extrusion foaming of low-density PE using azodicarbonamide as the blowing agent, and the studies conducted by Oyanagi and White[6] and Han and Villamizar[7] on the extrusion foaming of PS using azodicarbonamide or sodium bicarbonate as the blowing agent. Since chemical blowing agents are activated (decomposed) at higher temperatures, the foaming die block and extruder barrel nozzle can be selectively maintained at higher temperatures to initiate the decomposition of the blowing agent. The use of chemical blowing agents does not require very high pressures or pressure drops across the foaming die and hence running experiments using chemical blowing agents does not necessitate the use of elaborate and expensive high-pressure equipment. An excellent overview of foaming using chemical blowing agents is available in Han.[8]

Physical blowing agents are substances like simple gases (e.g., chlorofluorocarbons (CFCs), hydro chlorofluorocarbons (HCFCs), carbon dioxide (CO_2), nitrogen (N_2)), and some hydrocarbons (e.g., pentane, hexane), which are soluble in the matrix material at a certain pressure and temperature but become insoluble either when the pressure of the system is lowered or when the temperature of the system is changed.

Correspondence to: S. Shukla (shunahshep_03@yahoo.com).

Contract grant sponsors: NSF, Center for Advanced Polymer and Composite Materials.

Journal of Applied Polymer Science, Vol. 106, 1053–1074 (2007)

The bulk of the foaming in the polymer foam industry today is carried out using physical foaming agents (PFAs) since PFAs give higher volume expansion ratios and the phase separation times for PFAs are of the order of microseconds or milliseconds as against the decomposition half-life of the order of minutes for chemical blowing agents. Another advantage of PFAs is that they leave no solid residue in the final foam unlike chemical blowing agents, which leave more than 50% of their weight as residue. A number of studies have been conducted in recent years with PFAs for both batch[9–17] and continuous foaming.[8,17–34]

Conventionally, the polymer-foaming industry has been using CFCs and HCFCs for foaming, since these compounds have the highest solubility in most commodity plastics and yield foams with the highest volume expansion ratios. The foams using CFCs and HCFCs have cell sizes typically exceeding 100 μm and cell densities $\sim 10^6$ cells/cm^3 and are known as structural foam. Typical densities of extruded foam sheets are on the order of 5–50% of the base material. The primary application of PS structural foam is for building insulation and for producing styrofoam cups and take away food containers. However, because of the continuous pressure on the industry to move away from hazardous volatile organic carbons (VOCs) and ozone-depleting substances, there is great interest in exploring alternative, environmentally benign blowing agents such as CO_2 and N_2. CO_2 is a reasonably good PFA for the commodity plastics and there is interest in understanding the foaming process for polymer-CO_2 systems especially since the Kyoto protocol calls for banning CFCs and HCFCs as foaming agents by the year 2010—CFCs and HCFCs being detrimental to the ozone layer in the Earth's atmosphere.

Another reason for studying the foaming of polymers with inert gases such as N_2 and CO_2 is the possibility of producing microcellular foams using them. Microcellular foams are typically defined as foams having cell sizes less than ~10 μm and cell densities $>10^9$ cells/cm^3. Microcellular polymers have shown improved fatigue life and energy absorption, higher mechanical strength-to-weight ratio, higher impact strength and toughness, and higher thermal and dimensional stability when compared with structural foamed parts. Moreover, since the cells are so small, the foam possesses an excellent texture, and so, to an casual observer, the foamed plastic part retains the appearance of a solid plastic. Typical extruded foam densities for microcellular polymers are between 30 and 60% of the base material, and thus there is lesser material savings while using microcellular foams as compared to structural foams. So far, microcellular foams have been of greater interest to academia and to specialty foam producers but due to the safety hazards associated with potentially explosive alternative blowing agents like hydrocarbons and with the phase out of CFCs and HCFCs, there is increasing commercial interest in producing microcellular polymers. Experimental studies on foaming of polymers using CO_2 as the PFA has been an area of very active research in the last decade. Tomasko et al.[35] have provided an excellent review on the CO_2 applications in the processing of polymers.

Extrusion foaming of thermoplastics essentially comprises three main steps. The first step is the generation of a homogenous polymer-PFA solution in the extruder. Typically, polymer pellets are melted in an extruder and a metered amount of the PFA is injected at high pressure into the molten polymer through a gas injection port. Mixing of the polymer-PFA solution takes place via the process of convective diffusion.[29] In this process, the matrix material is stretched and folded by the action of flow in the screw channels while blobs of the injected gas in contact with the convecting polymer melt break up due to interfacial tension forces. The homogenization of the polymer-blowing agent solution is aided by the provision of mixing elements on the extruder screw downstream of the gas injection port or by provision of a static mixer following the extruder barrel or both.

The second step is the nucleation and growth of gas bubbles in a predominantly shear flow field. The pressure of a fluid element monotonically decreases as it moves along the die. Phase separation of the PFA from the thermoplastic matrix occurs following a small time period called the induction time or time lag of nucleation once the pressure of the polymer-PFA solution falls below the solubility limit of the PFA in the polymer. The nucleated bubbles continue to grow in the closed channel either under a shear flow field (if die diameter stays constant downstream of the saturation surface), or under a flow field where the elongational flow is superposed on the shear (if the shaping die has a different geometry than the foaming die).

The third and final step in extrusion foaming is the growth of the bubbles of the PFA in the cooling polymer foam exiting the die followed by freezing of the morphology once the temperature of the matrix material falls below its glass transition temperature. Most of the bubble growth in conventional foaming processes occurs during the extensional free surface flow of the extrudate exiting the die channel. The bubble growth, at least at lower temperatures (close enough to the glass transition temperature) is diffusion-driven, although at higher temperatures bubble coalescence and/or bubble collapse following an accelerated loss of gas to the surroundings may dominate the final foam morphology.[26,28,36]

Starting with the pioneering work of Prof Suh's group at MIT on the foaming of polymers with inert

gases (basically, N_2), extensive investigations on batch, semibatch, and continuous foaming processes using PFAs for both structural as well as microcellular foams have been carried out.[12,13,37] Since this article deals with continuous foaming of a thermoplastic using a PFA as the blowing agent through an extrusion capillary die, only the relevant literature is discussed in some detail below.

Han and Ma[20,21] performed experiments to determine viscosities of low-density PE and PS charged with fluorocarbon blowing agents using a capillary foaming die. They correlated their experimental data in terms of a viscosity reduction factor defined as the ratio of the viscosity of polymer-blowing agent mixture to that of the pure polymer melts. They demonstrated how their correlation could predict the viscosities of mixtures of low-density PE and PS charged with fluorocarbon blowing agents from data for the viscosity of the pure polymer melts alone.

Park et al.[27] investigated the effect of the pressure drop rate on cell nucleation in microcellular extrusion foaming of high impact PS with CO_2 as the blowing agent. Foaming was carried out in nozzles of different geometries (different radii and lengths) chosen such that for identical processing conditions and for the same amount of gas dissolved, the total pressure drop remained constant across each nozzle. The total number of cells nucleated was found to be a strong function of the pressure drop rate. The nucleation of a larger number of cells at higher pressure drop rates was attributed to the greater thermodynamic instability (higher solubility-drop rate) induced in polymer–gas solutions flowing through nozzles of smaller radii.

In a separate publication, Park and coworkers[34] employed a set of dies with differing geometries (capillaries with different lengths and radii) in a foaming extruder while systematically varying the concentration of blowing agent (CO_2) and nucleating agent (Talc) with PS (101, Nova Chemicals) as the matrix material. They also varied the die temperature from 170 to 120°C with a decrement of 5°C and also conducted experiments in which they varied the net pressure drop across the dies (while keeping the pressure drop rate constant). The authors observed that processing temperature had only a marginal effect on the cell density. They found that for all nucleating agent and blowing agent concentrations that they used, cell density increased significantly as pressure drop rate increased. However, changing the total die pressure across the foaming die (by altering either the die temperature or the die geometry) appeared to have no effect on the cell density, though it appeared to have a significant effect on the cell morphology of the obtained foams especially at low pressures (corresponding to higher CO_2 concentrations). The authors also found that the cell density increased with an increase of CO_2 concentration for all dies studied. Increasing the talc content was found to improve the cell density although the increase of the cell density with respect to the talc content was not high. The authors also observed that though the melt flowing near the wall of the die did not have a high pressure drop rate due to the retarded motion of the fluid close to the wall, the cell densities were observed to be slightly higher (up to 30% higher) than those of the core area in most cases. The higher cell density in the slowly flowing surface region was attributed to the nucleation induced by the shear action.

Han et al.[23,24] carried out experiments in which they carried out microcellular foaming of PS (685D) supplied by the Dow Chemical Company with CO_2 as the PFA. Experiments were carried out on an extruder equipped with a simple capillary foaming die to study the effects of the following key variables: foaming temperature, total pressure drop, pressure drop rate, and CO_2 concentration, on the final foam morphology in the PS-CO_2 system. Preliminary simulations were run using the computational fluid dynamics (CFD) package FLUENT to analyze the flow field in the foaming die. Since detailed viscoelastic scaling of the shear rheology data was not carried out for this work, the simulated results showed some discrepancies from experimental measurements.

The foaming of polymers is a complex process since it is controlled by a large number of process variables many of which are interdependent. Figure 1 depicts the dependence of the foam morphology on the material properties, operating variables, and field variables. The operator can choose the type of resin and the type of PFA to run on the process line and also the die geometry. The operator can also control the rate of heat exchange in various parts of the process line and the back pressure in the extruder (by provision of a gear pump, etc.) and set the throughput rates for the resin and the gas for the process.

Choice of a resin and PFA and setting the throughput rate together sets the material properties. The material properties and the basic field variables are interdependent as shown in Figure 1. Material properties show intricate dependencies on the amount of PFA dissolved and on the basic field variables. For example, the shear viscosity is a complex function of temperature, pressure, shear rate, and CO_2 weight fraction but these dependencies are known. However, the dependency of some material properties on the amount of gas dissolved in the polymer and on the basic field variables is not precisely known. For example, the dependency of thermal conductivity and specific heat capacity on shear rate or weight fraction CO_2 dissolved has not been systematically studied. The question mark ''?'' in front of a material parame-

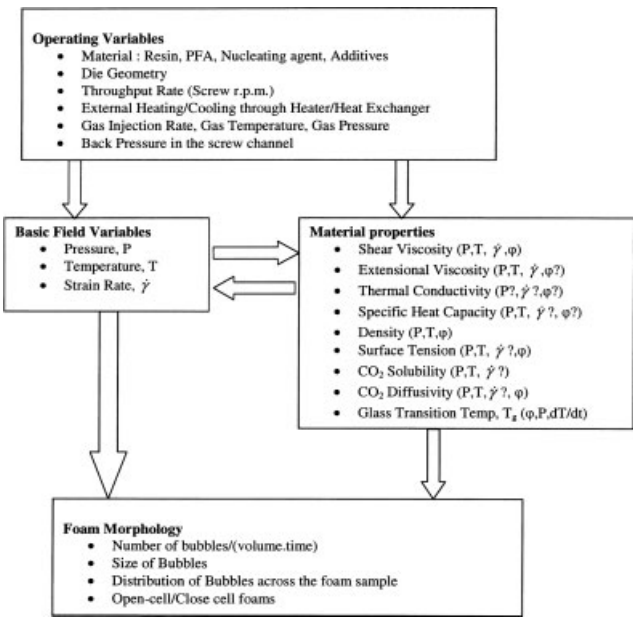

Figure 1 Summary of variables affecting final foam morphology in the foam extrusion process. Operating variables are ones that the experimenter/operator has control over. Material properties, both thermophysical and rheological, exhibit a strong dependence on the basic field variables—pressure, temperature, and shear rate as also on the diluent concentration in the melt. The question mark in the argument of a material property denotes an undetermined or unquantified dependency.

ter indicates such an unknown or unquantified dependency.

Since the polymer extrusion foaming process is one in which complex non-Newtonian flow is coupled with heat transfer, and involves unquantified material dependencies and also phase separation within the foaming die, modeling of the polymer blowing agent mixture through an extrusion foaming die has rarely been attempted. Commercial foam producing companies still resort largely to trial and error-based approaches when it comes to designing dies for new material formulations/ throughput rates. Such an approach is wasteful in terms of material and time. This work presents a simplified approach to modeling the flow of a polymer-PFA solution through an extrusion foaming die. In this work, an internally consistent viscoelastic scaling approach is adopted to simulate the axisymmetric contraction flow of a PS-CO_2 solution through an adiabatic extrusion foaming die using the CFD package FLUENT. In an internally consistent viscoelastic scaling approach, the temperature, pressure, and concentration corrections of viscosity are accounted for solely through their effect on the zero shear viscosity. This is the first time, to our knowledge, that simulations are being run for a polymer-blowing agent solution in an extrusion foaming die using an internally consistent viscoelastic scaling approach. The effects of die temperature and screw rotation rate (processing rate) on the temperature, pressure, and velocity profiles for an adiabatic foaming die are investigated in detail in this article for a constant CO_2 concentration of 1.0 wt % in PS. Reasonably good agreement is observed between the simulated and the experimentally measured pressure drops across the foaming die despite the assumption of a single phase PS-CO_2 solution flowing through the die over its entire length. The assumptions inherent in the simulation and the limitations of the work are discussed in the relevant sections throughout the article.

MODELING OF THERMOPHYSICAL PROPERTIES

Simulation of the extrusion foaming process requires the estimation of various thermophysical properties, viz., viscosity, thermal conductivity, density, and specific heat capacity for the polymer-blowing agent system under consideration. Of these viscosity estimation is the most important since viscosity can change by orders of magnitude with changes in shear rate, diluent concentration, and temperature and can also change significantly with pressure. In this work, a detailed methodology has been developed that integrates the concentration, temperature, and pressure shift of the viscosity with the shear rate dependence of the viscosity in an internally consistent manner. The approach is novel in that while previous researchers have largely focused on scaling down experimentally obtained high pressure polymer-blowing agent solution viscosity data onto a base curve for the viscosity of the undiluted polymer melt at a reference temperature and atmospheric pressure, we have succeeded in generating the shear viscosity data for our needs by scaling up the viscosity values obtained through a single set of experiments on the undiluted pure polymer melt at atmospheric pressure and using well-known correlations from the open literature. The power and the utility of the methodology lies in the fact that in principle from a single accurate viscosity-shear rate measurement conducted at a reference temperature and atmospheric pressure, it is possible to obtain the shear viscosity of the polymer-diluent solution for any arbitrary temperature, pressure, and diluent concentration in the processing window. Estimation of other thermophysical properties such as thermal conductivity, specific heat capacity, and density is also discussed below.

Viscoelastic scaling of PS-CO_2 solution

The viscosity of a polymer melt reduces appreciably when a suitable PFA is added to it. Data for polymer-PFA solution viscosities are difficult to obtain experimentally since the measurements have to be performed on elaborate high pressure systems

wherein the system pressure has to be maintained in excess of the degassing pressure of the PFA at all times to avoid the problems pertaining to phase separation in the system. As a result only a handful of data on PS-CO_2 systems are available in the open literature. Free-volume based arguments can be invoked to explain viscosity reduction of a polymer on addition of a PFA,[38–46] the paucity of data need not be a deterrent in carrying out simulations that can foster at least a qualitative (or even a semiquantitative) understanding of the mechanism of foaming in the extrusion die.

Gerhardt et al.[40,41] in their work with the poly(dimethyl siloxane) PDMS-CO_2 system demonstrated that classical viscoelastic scaling methods could be applied to reduce the PDMS-CO_2 solution viscosity curve to a master curve of pure PDMS. Kwag et al.[42,43] and later, Royer et al.[46] applied their viscoelastic scaling approach to PS-CO_2 systems to reduce their experimental viscosity data to a master curve of scaled viscosity $\eta(a_C\dot{\gamma})/a_C$ identical to the viscosity curve $\eta(\dot{\gamma})$ of pure PS at the same temperature and pressure. The authors reasoned that the PFA concentration scaling factor a_C ''corrects'' the viscosity of the polymer-CO_2 solution for the amount of CO_2 dissolved in the melt in the same way as the well-known temperature scaling factor ''corrects'' the viscosity for temperature or the pressure shift factor ''corrects'' the viscosity for the hydrostatic pressure imposed on the melt. Thus, to reduce their experimental viscosity curve for PS-CO_2 solution flowing through a capillary die, the authors first converted their apparent viscosity versus apparent shear rate data into a true viscosity versus true shear rate data through either a Rabinowitsch or Schuemmer[47] type correction and then computed pressure, temperature, and concentration shift factors such that when true viscosity/($a_T \times a_P \times a_C$) was plotted versus true shear rate $\times$ ($a_T \times a_P \times a_C$), the data collapsed perfectly onto the $\eta(\dot{\gamma})$ versus $\dot{\gamma}$ curve for the pure melt at the reference temperature (base temperature) and atmospheric pressure. Since in this study, ''scaling-up'' of the data from η ($T = T_{\text{ref}}$, $P = 1$ atm, $C = 0\%$ CO_2) to an η at an arbitrary T, P, and C within the foaming die was carried out, as opposed to the ''scaling-down'' done by the aforementioned authors to collapse their actual experimental data on PS-CO_2 solution flowing through a capillary die, an approach opposite to that prescribed by the above-mentioned authors in their publications was followed. The approach adopted is described in detail below.

Viscosity-shear rate data for pure PS melt was obtained on a parallel plate rheometer supplied by Rheometrics (RMS-800) and is shown in Figure 2. The data covered a broad temperature range (140–240°C, at 10°C intervals) encompassing the processing window on the foaming extruder and was measured as complex viscosity over three decades of frequency

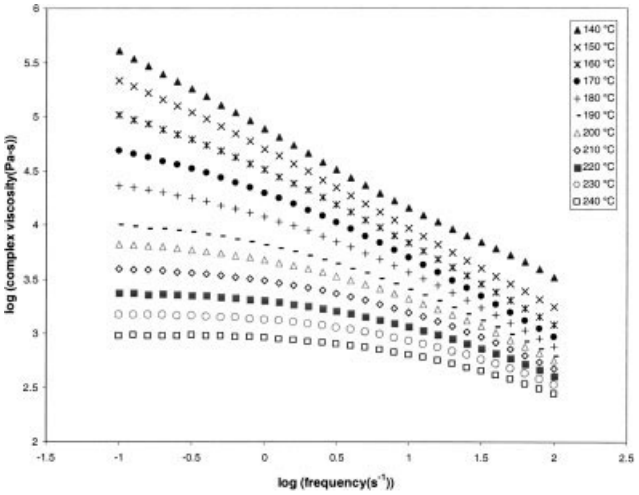

Figure 2 Measurement of complex viscosity of pure PS melt on the parallel plate rheometer (RMS 800) using small angle oscillatory shear at temperatures ranging from 140 to 240°C. The temperature range chosen is such as to encompass the extrusion temperature window over which foaming experiments had been previously conducted in our laboratory.

(0.1–100 s^{-1}, with 10 points per decade). According to the empirical Cox-Merz relationship, the shear rate dependence of the steady state viscosity is equal to the frequency dependence of the complex viscosity. Thus, 11 sets of data, from 140 to 240°C, with 30 points in each set viz. 330 points in all, were obtained via measurements conducted on the parallel plate viscometer and served as ''raw data.''

Once the raw data had been obtained, the first step in the formulation of a viscosity model for the PS-CO_2 system was to ascertain whether the kinetic bottleneck for molecular motions was the free-volume availability (in which case the data would fit a WLF type equation better) or whether the rate-limiting step for molecular mobility was an apparent activation energy for flow (wherein the Arrhenius relation would better fit the data). Williams et al.[48] in their original article on the WLF equation had cautioned that outside the range of 100°C above the T_g, the WLF equation could not be expected to hold for most glass-forming liquids. Their reasoning was that for ordinary glass-forming liquids far above their glass transition temperatures, specific details of molecular structure, through an apparent activation energy of flow, would dominate the flow behavior of the liquid, whereas in super-cooled liquids, in the range of about 100°C above their T_g, a ''universal'' temperature dependence, prescribed by the WLF equation, would overwhelm the specific structure-dependent differences and would control the flow behavior.

PS melt is an amorphous glass forming liquid but since the experimental data had been obtained over a temperature range extending beyond T_g + 100°C (the

T_g for pure PS at 1 atm pressure is 100°C), the experimental data was fit to both the Arrhenius relation[49] as well as to the WLF equation.[48] A far better fit was obtained when the WLF equation was used to fit the data over the entire temperature range. Next, a ''hybrid'' fit was attempted in which the WLF equation was used to fit the data in the temperature range of 140–180°C and the Arrhenius equation was used to fit the data over the temperature range of 200–240°C. The fit (in the normalized least-squares sense) was now found to be comparable with the case when the WLF fit was applied over the entire temperature range.

Reports of PS melt viscosities at higher temperatures in the literature are somewhat ambiguous[50,51] and there is no universal agreement regarding when the transition from the WLF temperature dependence to the Arrhenius temperature dependence of viscosity occurs. However, in a recent publication, Lomellini[50] argues that since PS has a bulky jumping unit, free volume is most likely the rate-limiting factor for molecular interactions over a wider temperature range than for ordinary glass-forming liquids. In fact, the author asserts that over the entire temperature range that he investigated (up to 290°C), the WLF free-volume description was uniformly obeyed for PS melt.

There is some evidence in the literature[52] that PS undergoes a slight decrease in the number–average molecular weight (M_n) between 180 and 220°C. However, this reduction is not significant enough to cause a noticeable change in the melt viscosity of PS for small processing times. Also, after the initial chain cleavages, no further reduction in M_n is observed for temperatures below 250°C.[53] Since the WLF fit is as good as the ''hybrid'' fit and since it would be more convenient to use a uniform temperature-dependence of viscosity descriptor over the entire temperature range, the WLF equation is used to describe the temperature dependence of PS melt over the entire processing window.

Temperature correction of viscosity

The WLF equation was used to implement the temperature correction of viscosity. The WLF equation can be written as:

$$\log(a_T) = \frac{-C_{1s}(T - T_s)}{C_{2s} + T - T_s} \tag{1}$$

where T_s is a reference temperature and C_{1s} and C_{2s} are the WLF constants. Williams et al.[48] recommend that T_s should be chosen around 50°C higher than the T_g of the liquid (i.e., about the middle of the range over which the WLF equation is valid) to get the most appropriate values of C_1 and C_2 for shifting.

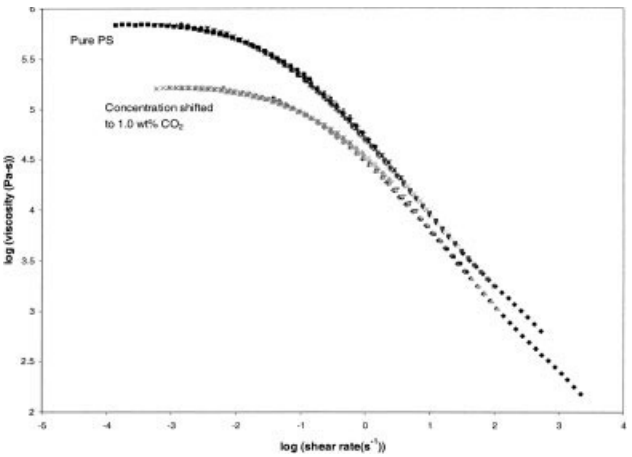

Figure 3 The upper curve shows time-temperature superposition of the complex viscosity data of Figure 2 with a view to obtain the shift factor for each temperature with the 150°C curve serving as a reference. The lower curve depicts the concentration shift of the data of the upper curve were it possible to dissolve 1.0 wt % CO_2 into the pure PS melt at atmospheric pressure and at 150°C temperature.

Figure 3 shows the time-temperature superposition of the small angle oscillatory shear data of Figure 2. The reference temperature, T_s, is chosen to be 150°C for the shift, since it provides the best C_1 and C_2 values to shift the viscosity to other temperatures—larger deviations are observed between the shifted viscosity and the measured viscosity for all other choices of reference temperature T_s. Starting with the reference curve, the shear viscosity curves in Figure 3 for different temperatures are superposed on each other to obtain the value of a_T for each temperature. A plot of $T - T_s/(\log a_T)$ vs. $(T - T_s)$ then gives a straight line with slope s and intercept i such that[54]:

$$C_{1s} = -1/s \tag{2a}$$

$$C_{2s} = i/s \tag{2b}$$

Once C_{1s} and C_{2s} corresponding to the reference temperature T_s are obtained, C_{10} and C_{20}, corresponding to any arbitrary reference temperature T_0 can be obtained simply by using the relations[48,55]:

$$C_{20} = C_{2s} + T_0 - T_s \tag{3a}$$

$$C_{10} = (C_{1s}C_{2s})/C_{20} \tag{3b}$$

In this manner, the values of C_{1g} and C_{2g}, corresponding to the glass transition temperature, T_g, are obtained. The values of C_{1g} and C_{2g} so obtained over the usual range of validity of the WLF equation are 13.28 and 48.53, respectively, which compare favorably with the values cited in the literature.[54] For the

range T_g + 100°C to T_g + 140°C, C_{1g} and C_{2g} are obtained as 13.45 and 37.21, respectively. Use of these values for the concentration shifting of the viscosity data is described in the next section.

Concentration correction of viscosity

Following Royer et al.[46] and Kwag et al.,[42] the concentration shift factor was computed using the basic notion that the combined shift factor ''a'' can be written down as a product of the individual scaling shift factors for temperature (a_T), pressure (a_P), and concentration (a_C). Thus,

$$a = a_T a_C a_P$$

Therefore,

$$\log(a) = \log(a_T a_C a_P) = \log(a_T) + \log(a_C) + \log(a_P)$$

Since concentration scaling is carried out first on the raw data at atmospheric pressure, $a_P = 1$ and the above equation becomes

$$\log(a_C) = \log(a_T a_C) - \log(a_T)$$

Therefore,

$$\log(a_C) = \frac{-C_{1g,\mathrm{mix}}(T - T_{g,\mathrm{mix}})}{C_{2g,\mathrm{mix}} + T - T_{g,\mathrm{mix}}} + \frac{C_{1g}(T - T_g)}{C_{2g} + T - T_g} \quad (4)$$

where, a_C is the concentration shift factor, C_{1g} and C_{2g} are the WLF constants for the pure polymer and $C_{1g,\mathrm{mix}}$ and $C_{2g,\mathrm{mix}}$ are the WLF constants for the PS-CO_2 solution, which may or may not be equal to C_{1g} and C_{2g}. $T_{g,\mathrm{mix}}$ refers to the glass transition temperature of the PS-CO_2 mixture were it possible to dissolve the prescribed amount of CO_2 into the PS melt at atmospheric pressure.

Only a few models are available in the literature to predict T_g depression on addition of a diluent for different polymer-diluent systems. For the PS-CO_2 system, two models are in popular use—the robust but slightly complex model of Condo et al.[56] and the simple but approximate model of Chow. For the purpose of this work, $T_{g,\mathrm{mix}}$ is computed using the Chow model,[57] which gives reasonably valid estimates of T_g depression for PS-diluent systems, at least at low concentrations of CO_2 in the melt. The Chow model is based on the mean-field (Braggs-Williams) approximation for lattice fluid mixtures. In the Braggs-Williams approximation, originally derived for a lattice gas,[58] the configurational degeneracy and average nearest neighbor interaction energy are both handled assuming a random distribution of molecules among sites (implying a nearest neighbor energy of 0). The Chow model can be expressed as

$$\ln\left(\frac{T_g}{T_{g,\mathrm{mix}}}\right) = \beta[(1-\theta)\ln(1-\theta) + \theta \ln\theta] \quad (5)$$

In the above equation, β and θ are dimensionless parameters defined as

$$\beta = \frac{zR}{M_p \Delta C_{\mathrm{pp}}}, \quad \theta = \frac{M_p\, w}{zM_d\,(1-w)}$$

where, M_p and M_d refer to the molecular weight of the monomer and the diluent, respectively, ΔC_{pp} is the excess transition isobaric specific heat of the polymer, w is the mass (or weight) fraction of the diluent, z is the lattice coordination number, and R is the gas constant. Addition of a small amount of diluent in a polymer mainly affects θ, β being usually fixed for a given polymer. Chow used a value of 2 for z to compare his theory with experimental data for various PS-diluent systems and found that his model predicted T_g depressions reasonably well for the diluents considered.

Chiou et al.[59] used differential scanning calorimetry to estimate the glass transition temperature of many polymer-diluent systems (including PS-CO_2 solution). They found that the Chow model with a value of z = 1 could fit their PS-CO_2 $T_{g,\mathrm{mix}}$ data better than the z = 2 case. Following Chiou et al.,[59] a value of z = 1 was adopted to calculate the T_g depression of PS on addition of CO_2 along with the following values for the other model parameters: T_g = 100°C, M_p = 104 g/mol, ΔC_{pp} = 0.0767 cal/(g °C), w = 0.01, M_d = 44.06 g/mol, R = 1.987 cal/(mol °C). The value of $T_{g,\mathrm{mix}}$, corresponding to 1.0 wt % CO_2 in PS was found to be 89.67°C. Using this value of $T_{g,\mathrm{mix}}$, a_C was computed using eqs. (4) and (5). The time-temperature superposed data for pure PS in Figure 3 was then concentration shifted to the 1.0 wt % CO_2 data in Figure 3 using the computed value of the shift factor a_C.

Pressure correction of viscosity

The effect of pressure on the capillary flow of PS melt has been investigated by many researchers.[60–64] Penwell and Porter[63] carried out experiments on nearly monodisperse ($M_w/M_n < 1.10$) low molecular weight (20,400) and high molecular weight (670,000) PS fractions flowing through a capillary. The low molecular weight PS fraction was chosen since viscous dissipation could be assumed to be negligible for it and since it gave no indication of elastic energy storage (as evidenced by insignificant die swell and small entrance losses) at low enough rates of flow through the capillary dies. Thus, the pressure effect could be more readily segregated once the flow rates were increased. The high molecular weight PS fraction was chosen

since it resembles better the real PS melt flowing through most commercially relevant geometries. The authors showed that for the low molecular weight material, the application of a WLF type correction (through an accounting of the T_g elevation due to pressure, evaluated at the mean pressure of the flow) sufficed to explain the pressure effect on viscosity. For the higher MW material, though, application of a WLF type correction after correcting for entrance and die-swell effects greatly overpredicted the viscosity. The authors rightly attributed the overprediction to ignoring the shear-thinning of the polymer due to viscous heat generation for the higher molecular weight PS fraction. Accounting for the shear-dependence of viscosity separately would enable a WLF type correlation to correct for the PS melt viscosity at high pressures. As in the case of concentration correction of the viscosity, the pressure correction was also implemented through accounting for a change in T_g of the polymer melt with the affecting variable (here pressure).

Thus, for a specified CO_2 concentration in PS, one can write, following Penwell et al.[64] and Royer et al.[46]:

$$\log(a_P) = \log(a_P a_T) - \log(a_P)$$

Therefore,

$$\log(a_P) = \frac{-C_{1g,\mathrm{mix}}(T - T_{g,\mathrm{mix},P})}{C_{2g,\mathrm{mix}} + T - T_{g,\mathrm{mix},P}} + \frac{C_{1g,\mathrm{mix}}(T - T_{g,\mathrm{mix}})}{C_{2g,\mathrm{mix}} + T - T_{g,\mathrm{mix}}} \tag{6}$$

Many researchers have investigated the effect of pressure on the T_g of polymer melts. There is a pretty good agreement between the various bodies of research that for pressures routinely encountered in polymer processing operations such as extrusion and injection molding, T_g increases linearly with pressure. Following Penwell et al.[64]:

$$T_{g,P} = T_{g,P_0} + A_1 \cdot P$$

where $A_1 = \frac{\partial T_g}{\partial P}$ is the pressure coefficient of viscosity.

Several researchers have determined the value of the coefficient A_1[65,66] and these values typically fall in a pretty narrow range (0.28–0.31 K/MPa). The value of 0.29 K/MPa determined by Quach and Simha[66] was used for our calculations.

Figure 4 depicts the relative importance of pressure and concentration shifting of viscosity at an arbitrarily chosen temperature and pressure in the processing window for the PS-CO_2 solution. It can be clearly seen that the concentration shift of viscosity is much more pronounced than the pressure shift, even for a CO_2 concentration of as little as 1.0 wt % in PS. However, as our simulation results reveal later, at a fixed diluent concentration in the melt, the pressure dependence of viscosity can play a significant role in determining the flow behavior, and should not be ignored in flow simulations within extrusion dies and injection-molding gates and runners.

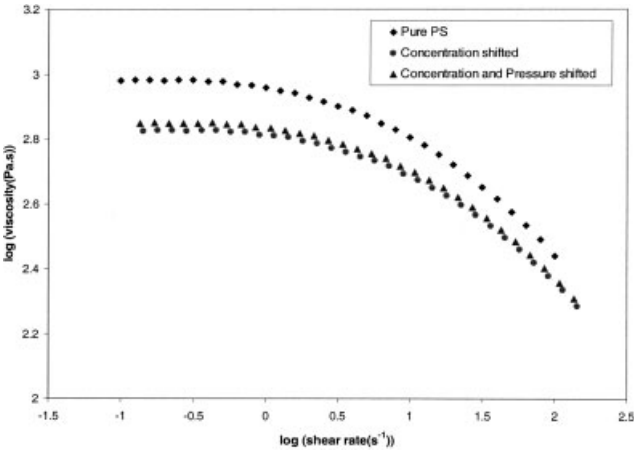

Figure 4 Relative importance of concentration and pressure shifting of viscosity at a temperature of 240°C and a mean pressure of 5.65 MPa. Pure PS data is at T = 240°C and P = 1 atm. Concentration shifted data is the reduced viscosity data that would be obtained were it possible to dissolve 1.0 wt % CO_2 in PS at T = 240°C and P = 1 atm. Concentration and pressure shifted data is at T = 240°C and P = 5.65 MPa. The plot shows that even for as low as 1.0 wt % CO_2 dissolved in PS, the viscosity change induced by CO_2 dissolution is much more significant than that brought about by pressure imposed in the die under typical extrusion foaming conditions.

Shear-rate dependence model for the viscosity of PS-CO_2 solutions

To represent the shear-rate dependence of the shear viscosity of polymer melts, Hieber and Chiang[67] suggest the use of the following functional form, which is a generalization of the popular models of Cross and Carreau:

$$\eta = \frac{\eta_0}{\left[1 + \left(\frac{\eta_0 \dot{\gamma}}{\tau^*}\right)^c\right]^{\frac{(1-n)}{c}}} \tag{7}$$

In this model, η_0 represents the zero-shear-rate Newtonian viscosity and n, τ^*, and c are model constants. Equation (7) reduces to the cross model for $c = 1 - n$, to the Carreau model if $c = 2$ and to the ''modified Carreau model'' if $c = 1$. The parameter c characterizes the breadth of the transition between the Newtonian and power law regimes of the viscosity dependence on shear, being broadest for the Cross model ($c = 1 - n < 1$), less broad for the modified Carreau model ($c = 1$) and narrowest for the Carreau model ($c = 2$). Since the breadth of the transition between the Newtonian and power law regimes is

narrower for narrow molecular weight distribution and wider for broad molecular weight distributions, the Carreau model is expected to better fit the narrow molecular weight distribution case while the Cross model is likely to be more appropriate for the broad molecular weight distribution case. The Cross, modified Cross, and Carreau models were used to fit the experimental data for the commercial PS (PS Dow 685D) on which rheological measurements had been made on the parallel plate rheometer. The Cross model was found to give a better fit of the data than the Carreau model. The generalized Cross–Carreau model with an additional parameter, *c*, was found to give slightly better fits of the data than the Cross model, but since the Cross model also gives an excellent fit of experimental data over a wide shear rate range, has a minimum number of independent constants and since each of the constants in the Cross model possesses a physical significance, the Cross model was chosen to fit the viscosity shear-rate data.

Cross derived his model to fit experimental data for a number of non-Newtonian fluid systems (including undiluted polymer melts). His model can be expressed in the following form[68]:

$$\eta = \eta_\infty + \left(\frac{\eta_0 - \eta_\infty}{1 + \alpha\dot{\gamma}^m}\right) \tag{8}$$

where, η_∞ is the value of the ''infinite shear rate'' viscosity observed in the second Newtonian regime, and α and m are model constants. The above equation was used to fit the concentration-reduced-viscosity-data to get an initial estimate of the zero shear viscosity corresponding to the highest temperature (for which the zero-shear Newtonian plateau could be most distinctly observed).

Vinogradov and Malkin[69,70] investigated the temperature-independent viscosity characteristics of polymer systems. On the basis of molecular theories concerning the temperature dependence of the viscoelastic properties of polymers,[71] the authors arrived at the following functional form of the dependence of viscosity upon the shear rate:

$$\frac{\eta}{\eta_0} = f\left(\dot{\gamma}\eta_0(T)\right)$$

The temperature dependence of the shear viscosity of polymers is thus accounted for solely through its effect on the zero shear viscosity and can now be accommodated into the Cross model by writing it in the following form:

$$\eta = \frac{\eta_0}{\left[1 + \left(\frac{\eta_0\dot{\gamma}}{\tau^*}\right)^{1-n}\right]} \tag{9}$$

where τ^* is a constant. For high enough shear rates, the above equation can be reduced to the power-law model with n representing the flow behavior index. A plot of $\frac{\eta}{\eta_0}$ vs. $(\dot{\gamma}\eta_0(T))$ allows one to scale out the temperature (and likewise pressure) dependence of η and thereby to isolate the shear-rate dependence alone. Figure 5 shows the result of applying such a scaling on master-plot coordinates for 1.0 wt % CO_2 in PS. The data points show good superposition on the master-coordinates and the Cross model fits the superposed data very well. The value of the constants in the Cross model obtained through this procedure are $\tau^* = 25224.86$ and $n = 0.2462$.

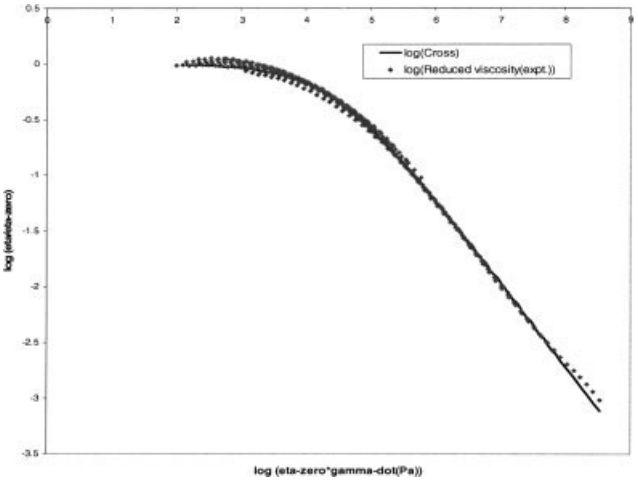

Figure 5 Concentration shifted viscosity data plotted on Master Coordinates (reduced viscosity versus reduced shear rate). The plot enables the determination of the Cross model parameters n and τ^* in such a manner that the zero shear viscosity can acquire values, which are consistent with both the WLF equation and the Cross model simultaneously.

Note that the ''infinite shear rate'' viscosity has been taken to be zero in eq. (9). Takahashi et al.[72] have carried out experiments to measure the viscosity of pure PS melt at very high shear rates (up to 10^8 s^{-1}) using a specially designed high-shear-rate rheometer. They observed that the second Newtonian region was not observed for PS melts, instead a transition region was observed over which dual values of the apparent viscosity were obtained at one shear rate. Beyond a shear rate of 10^6 s^{-1}, the apparent viscosity was measured to be only $\sim$ 1 Pa s at 230°C. Since the η_∞ is so low and since no appropriate correlation is available in the open literature to estimate the ''infinite shear rate'' viscosity, η_∞ is taken to be zero in eq. (9).

Figure 6 shows a comparison of the concentration shifted viscosity data (points) with the Cross model predictions (full curves). The Cross model gives a very good fit of the data and isolating the temperature effect in the zero-shear viscosity ensures no cross-over of the curves at higher shear rates.

Thermal conductivity

Little is known about the dependence of thermal conductivity on the shear rate or weight fraction gas

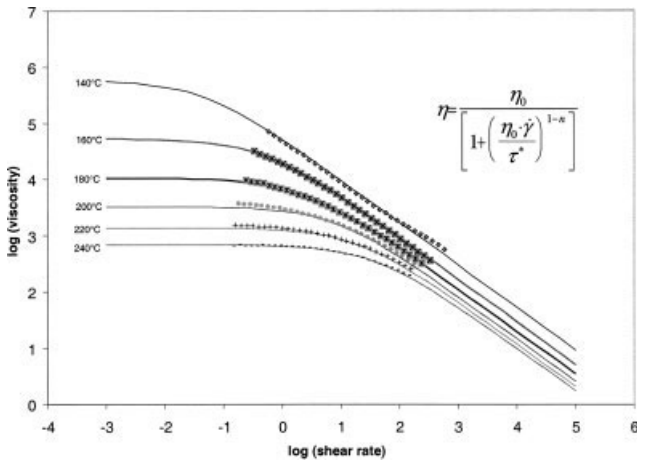

Figure 6 Comparison of the concentration shifted viscosity data with the Cross model predictions and extension of the Cross model prediction to higher shear rates value typically encountered in commercial extrusion dies.

dissolved for polymer-blowing agent solutions. Experimental measurements of anisotropic thermal conductivity in a flowing polymer melt are scarce in the open literature and somewhat ambiguous. Picot and his coworkers[73,74] measured the effective thermal conductivity for a commercial polydimethyl siloxane sample and a PE sample of high molecular weight and found that the thermal conductivity increased in the flow direction at higher shear rates. Venerus et al.[75] studied anisotropic thermal conduction in a polyisobutylene melt following a step shear deformation. They observed that the thermal conduction was enhanced in the flow direction and reduced in the neutral (or vorticity) direction, relative to the equilibrium level.

Since no thermal property estimates were available for PS-CO_2 solutions in the literature, corresponding values under the prescribed processing conditions for pure PS were used for our simulations. Sakakibara et al.[76] estimated the thermal conductivity of pure PS above and below the glass transition temperature. For a temperature range between 416 and 513 K for a PS sample with a viscosity average molecular weight in the range of 141,000–148,000, they estimated the thermal conductivity to be 0.1659 W/(m K) to a maximum deviation of 1.2% in the measured values. This value was obtained under static conditions and was the one chosen for our simulations.

Density

The Sanchez-Lacombe equation of state (SLEOS) which is based on the lattice fluid theory of polymer solutions gives reasonable approximations of the density of many polymer-diluent mixtures[77] and gives very good estimates of the density of PS-CO_2 solutions under normal processing conditions for the mixture.[35] The SLEOS can be expressed as:

$$\tilde{\rho}^2 + \tilde{P} + \tilde{T}[\ln(1-\tilde{\rho}) + \tilde{\rho}] = 0 \tag{10}$$

where $\tilde{\rho}$ is the reduced density ($\tilde{\rho} = \rho/\rho^*$), $\tilde{P}$ is the reduced pressure ($\tilde{P} = P/P^*$), $\tilde{T}$ is the reduced temperature ($\tilde{T} = T/T^*$). The equation-of-state parameters for the mixture ρ^*, P^*, and T^* are computed from the corresponding pure-component values using conventional (though somewhat arbitrary) mixing rules. Sato et al.[78] measured the solubility of carbon dioxide in PS using a pressure decay method for temperatures ranging from 373.2 to 453.2 K and for pressures up to 20 MPa. They used the following values of characteristic parameters: $P^* = 720.3$ MPa, $\rho^* = 1580$ kg/m^3, $T^* = 269.5$ K for PS and $P^* = 1036$ MPa, $\rho^* = 803.4$ kg/m^3, $T^* = 159$ K for CO_2. The mixing rules that we used in this work can be expressed following Sato et al.[78] as

$$P^* = \sum_i \sum_j \varphi_i \varphi_j P^*_{ij} \tag{11}$$

$$P^*_{ij} = (1 - k_{ij})\left(P^*_i P^*_j\right)^{0.5} \tag{12}$$

$$T^* = P^* \sum_i \left(\varphi_1^0 T^*_i / P^*_i\right) \tag{13}$$

$$1/r = \sum_i \left(\varphi_i{}^0 / r_i^0\right) \tag{14}$$

$$\varphi_i^0 = \left(\varphi_i P_i{}^* / T_i^*\right) \Big/ \sum_j \left(\varphi_i P_j^* / T_j^*\right) \tag{15}$$

$$\varphi_i = \left(w_i/\rho_i^*\right) \Big/ \sum_j \left(w_j/\rho_j^*\right) \tag{16}$$

where $T_i{}^*$, $P_i{}^*$, ρ^*, and r_i^0 are the characteristic parameters of ith component in the pure state. The temperature-dependent binary interaction parameter k_{ij} in the mixing rules was determined by minimizing the relative deviations between experimentally measured and SLEOS predicted solubility measurements for the PS-CO_2 system and can be expressed in the following form[79]:

$$k_{ij} = -0.0005T + 0.1149 \tag{17}$$

where k_{ij} is the only interaction parameter that is used in fitting SLEOS to laboratory measurements. It accounts for the ''non-idealities'' of the binary system (for example, the heat and volume changes of mixing) of the two components.

Specific heat capacity

No data on specific heat capacity of PS-CO_2 mixtures is available in the open literature. Also, little is known about the change in heat capacity on application of a

shear field. It is known that heat capacity depends on the internal degrees of freedom of a polymer fluid[80] but since this configurational dependence has not been quantified, C_p data on pure PS under static conditions from Karasz et al.[81] was fitted to obtain the C_p values that we used in our simulations. The specific heat capacity was found to vary linearly with temperature according to the following equation under prescribed processing conditions:

$$C_p = 3.2723T + 612.53 \tag{18}$$

where C_p is the specific heat capacity in J/(kg K) and T is the temperature in K.

CFD MODELING TECHNIQUE

The die geometry consists of a die insert, which has a length of 56.12 mm and an internal diameter of 7.8 mm followed by the foaming capillary die, which has a length of 10 mm and an internal diameter of 0.5 mm. However, since most of the important flow physics occurs in the capillary die and since the flow in the die insert far upstream of the contraction does not significantly affect the flow in the capillary die, only 23.4 mm of the guiding hollow tube (die insert) and 10 mm of the foaming die were simulated. Such a selective elimination of volume is very desirable from the point of view of computational economy and significantly aids mesh refinement and data analysis in FLUENT. The geometry of interest is displayed in Figure 7(a).

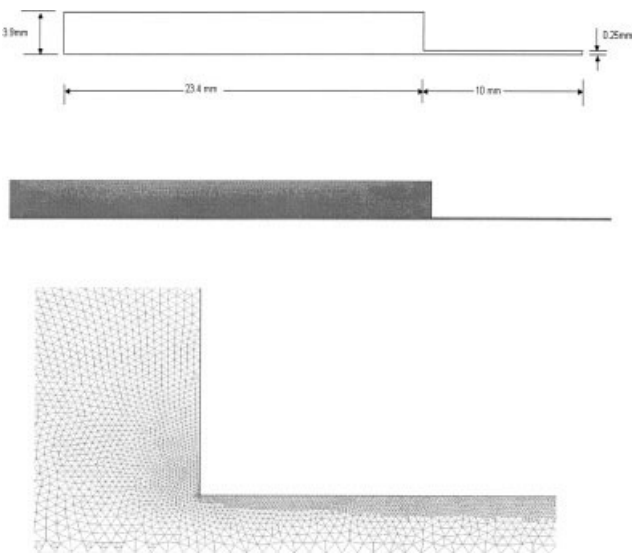

Figure 7 (a) Top: Geometry of the contraction. Since the die is axisymmetric, only the symmetric part of the 2D geometry needs to be meshed. (b) Middle: Diagram showing the mesh. The mesh has ~ 76,000 triangular cells (~ 40,000 nodes). Since the mesh is very fine, it is hard to observe individual cells. (c) Bottom: Enlarged view of the grid near the contraction. Grid adaption based on temperature gradients has been carried out in the region near the wall and near the entrance corner.

The mesh is created on the preprocessor GAMBIT (version 2.0.4). Figure 7(b) displays the mesh. The mesh as created in GAMBIT contains ~ 61,000 triangular cells. Further refinement of the mesh is carried out in regions of high temperature gradients near the entrance corner and the walls of the foaming die—a process called grid adaption. An enlarged view of the adapted mesh near the entrance corner is shown in Figure 7(c).

The steady, two-dimensional, axi-symmetric, segregated solver formulation incorporating an implicit discretization scheme was used to solve the flow problem in FLUENT. The two dimensional double-precision solver was chosen in FLUENT to model the die geometry. The double-precision feature of the solver enhances the numerical accuracy of the solution. Since the liquid flows from a capillary of relatively large diameter, through an abrupt contraction, and into a capillary of smaller diameter, the axisymmetric (x,r) formulation of the equations of change is used. The advantage of using this formulation is that the three-dimensional (x,y,z) problem in Cartesian coordinates is reduced to a 2D (x,r) problem in cylindrical coordinates while still retaining most of the essential physics of the 3D (x,y,z) problem. This simplifies the meshing of the geometry considerably, makes it much easier to extract and interprets the simulation data, and substantially speeds up the iteration process (so that the solution converges in a matter of hours instead of converging in days).

The conservation equations were cast in the following form given in tensor notation:

Mass Conservation Equation (Continuity Equation):

$$\nabla \cdot (\rho \underline{v}) = 0 \tag{19}$$

where ρ is the mass density, and $\underline{v}$ is the velocity vector.

Momentum Conservation Equation:

$$\nabla \cdot (\rho \underline{v}\underline{v}) = -\nabla p + \nabla \cdot \left(\underline{\underline{\tau}}\right) \tag{20}$$

where p is the pressure and $\underline{\underline{\tau}}$ is the stress tensor.

Energy Conservation Equation:

$$\nabla \cdot \left(\underline{v}(\rho E + p)\right) = \nabla \cdot \left(k\nabla T + (\underline{\underline{\tau}} \cdot \underline{v})\right) \tag{21}$$

where k is the thermal conductivity and E is the internal energy given as:

$$E = h - \frac{p}{\rho} + \frac{v^2}{2}$$

where h is the sensible enthalpy which for incompressible flows is defined by:

$$h = \int_{T_{\text{ref}}}^{T} Cp\, dT + \frac{p}{\rho}$$

where T_{ref} is a reference temperature.

In the finite volume method, the numerical algorithm is implemented through three steps.[82] The first step is formal integration of the governing equations of fluid flow and heat transfer over all the (finite) control volumes or cells of the solution domain. The second step is the substitution of a variety of finite-difference-type approximations for the terms in the integrated equation representing flow processes. And the third step is the solution of the algebraic equations by an iterative scheme. The efficiency of the solution for the segregated solver in FLUENT is enhanced by using the Algebraic Multi-Grid (AMG) scheme in conjunction with the Gauss–Siedel method.

The materials panel in FLUENT was used to feed in the thermophysical properties, k and C_p and the bulk density, ρ for the fluid into the simulation. The density of the fluid varies only by a very small extent over the flow length in the die for the pressure conditions used (only around 1% variation in density for the maximum pressure drop under the simulation conditions studied). Therefore, for the purpose of this simulation, variations in density were ignored and the fluid was assumed to be incompressible. The SLEOS was used to compute for the density at the entrance of the die geometry and it was this density, which was used to compute the inlet velocity of the fluid for the simulation. The pressure and temperature corrections of the concentration-shifted viscosity were incorporated into the simulation in a dynamic way by writing appropriate user defined functions and linking them to the FLUENT solver.

Convergence of the solutions was tested using two approaches. The first approach was to decrease the grid spacing in regions of high gradients (such as corners and walls), viz. selective mesh refinement via grid adaption. The second approach was to place more stringent criteria on the mass, momentum, and energy residuals than the default criteria in FLUENT. In all cases, the default criteria for residuals in FLUENT were found to be inadequate for convergence. Also, decreasing the grid spacing caused no change in the solution properties at lower flow rates and/or higher temperatures but mesh refinement through grid adaption based on temperature gradients caused significant change in the solution properties at lower temperatures and/or higher flow rates.

The SIMPLEC (SIMPLE Consistent) Algorithm was used for the pressure-velocity coupling. The acronym SIMPLE stands for Semi-Implicit Method for Pressure-Linked Equations and is essentially a guess-and-correct procedure for the calculation of pressure on the staggered grid arrangement in FLUENT. The SIMPLEC method is a refinement of the SIMPLE method that enhances the economy and stability of the simulation. The Second-Order Upwind differencing scheme, which fulfils the requirements of conservativeness, boundedness, and transportiveness, was used for discretization of the governing equations. Since the flow is not aligned with the grid lines for our geometry, the distributions of transported properties tend to become smeared—a process referred to as false diffusion. Selective mesh refinement and use of a higher order differencing scheme minimizes, but does not completely eliminate smearing. The resulting error due to false diffusion is expected to be small, but an exact assessment of the error still needs to be made. Finally, a judicious choice of underrelaxation factors for the continuity, momentum as well as energy equations had to be made for all our simulations. The underrelaxation factors for momentum and energy, especially, had to be assigned very low values initially but could be gradually incremented, as the solution proceeded, to speed up the convergence of the solution.

Assumptions inherent in the mathematical model

An important assumption that has been made to simplify our computations was that the formation of a two-phase mixture beyond the saturation surface in the die, does not significantly affect the profiles of the field variables (temperature, pressure, and shear-rate) in the die. This assumption was made to simplify the physics of the problem and avoid the problems arising from phase separation on the flow physics. Although this might appear as a severely limiting assumption at first glance, two points must be mentioned which go in its favor. (1) The average time that a fluid element spends in the die downstream of the saturation surface is only $\sim$ 0.015 s at low processing rates (corresponding to 10-rpm screw rotation rate) and lesser still at higher processing rates. Such a short time comprises a very small fraction of the total bubble growth time of 2–10 s documented in numerous studies on bubble growth. Such short residence times are typical of continuous microcellular foaming processes, which require very high pressure drop rates for bubble nucleation densities to approach the microcellular regime. (2) In many studies of bubble nucleation, a time period of the order of microseconds or milliseconds (depending on the system being studied) has been observed from the time when the nucleation is thermodynamically favored to the time when critical nuclei actually appear. This time period is called the time lag of nucleation, and so far as we know, experimental data on the time lag of nucleation in polymer-supercritical diluent systems is not available. Moreover, it has been noted that the phase-separation kinetics in the case of polymer foaming are often slow enough to differentiate between the formation of a single phase metastable state from the subsequent nucleation and growth stages so that the pressure drop step can be modeled as a single phase, multicomponent adiabatic pressure

drop.[83] Thus, the assumption of approximating the flow as a single phase flow throughout the capillary die length might not be very unreasonable for microcellular foaming through extrusion dies and can give useful insights into the dynamics of flow in a nonisothermal foaming die.

A second assumption that has been made is that the fluid flow is laminar and steady state at all times. The laminar flow assumption is justified on the basis of the very low Reynolds numbers (<1) prevailing in the flow system at any point in the capillary die.

It is widely accepted in the polymer-processing community that polymer melts, unlike Newtonian fluids, may violate the classic no-slip boundary condition when the shear stress exceeds a critical value (usually about 0.1 MPa). Shidara and Denn[84] studied the slip behavior of PE and PS through very thin slit dies (gaps ranging between 34 and 765 μm). They reported that while slip was exhibited at the wall for the PE melt, no slip was observed for the PS melt under similar processing conditions. Later on, Rosenbaum and Hatzikiriakos[85] carried out a numerical analysis for a hypothetical PS fluid and suggested, based on their numerical results, that slip could be occurring in the experiments conducted by Shidara and Denn[84] on PS, but since viscous heating in the case of PS is significant, it could be dominating the wall-slip effect for the polymer. However, although Rosenbaum and Hatzikiriakos[85] procured experimental data for LDPE, HDPE, and PP to demonstrate the agreement of their model predictions with experimental data, they have not carried out experiments to corroborate the wall slip effect for PS. For simplicity, and in want of more conclusive data, the no slip condition has been imposed at the wall for all our simulations.

Although normal stresses could be important in contraction flows and especially through capillaries of small length (where the flow time could well be comparable to the characteristic polymer segment relaxation time), this article considers only shear stresses. Also, the effect of gravity on flow has been assumed to be negligible.

RESULTS AND DISCUSSION

Continuous microcellular foaming of PS-CO_2 mixtures at 1.0 wt % blowing agent concentration had been carried out earlier in our laboratory at two different screw rotation rates, 10 and 30 rpm. For the lower screw rotation rate of 10 rpm, foams had been produced for inlet melt temperatures (into the die insert) corresponding to 140, 160, 180, 200, 220, and 240°C. For the higher screw rotation rate of 30 rpm, foams had been produced for inlet melt temperatures corresponding to 160, 180, 200, 220, and 240°C. Processing at 140°C for the higher screw rotation rate of 30 rpm was not carried out due to the pressure limitations of the die. Table I summarizes the process conditions for extrusion foaming of PS-CO_2 solution carried out in our laboratory. The experimental setup and results have been discussed earlier in detail by Han et al.[24] The velocities and temperatures listed are the inlet velocities and temperatures of the homogenous fluid stream entering the die insert. In the discussion that follows, the focus is on the simulation results and on the comparison of the experimental findings and the model predictions. Note that in the discussion below, the low processing rate always corresponds to 10 rpm screw rotation rate and the high processing rate always corresponds to 30 rpm screw rotation rate. Also, the temperatures correspond to the inlet melt temperature of the polymer entering the die insert, unless otherwise specified.

Pressure drop across the die

The pressure drop profiles along the die for the low flow rates (corresponding to 10 rpm screw rotation rate) for all the different inlet temperatures studied are shown in Figure 8. Several features of interest can be observed from the figure. Most of the pressure drop occurs in the thin capillary region of the foaming die. The pressure in the die insert stays almost constant for all inlet melt temperatures studied; even for the case of the lowest temperature, 140°C, (corresponding to the highest viscosity), only a very small fraction of the total pressure drop occurs in the die insert. The pressure profile along the capillary is highly nonlinear. Pressure drops appreciably in the initial entrance section of the capillary and falls less steeply in the region of the capillary away from the contraction. The total pressure drop in the die is a sensitive function of the inlet melt temperature and the sensitivity increases as temperature decreases. Pressure contours were also obtained to analyze the radial variation in pressure at a given axial location—

TABLE I
Summary of Process Conditions for Extrusion Foaming of PS-CO_2 Solution

Temperature (°C)	Velocity at 10 rpm screw rotation rate (m/s)	Velocity at 30 rpm screw rotation rate (m/s)
140	0.0010219	
160	0.0013164	0.0048546
180	0.0013534	0.0038688
200	0.001562	0.0044833
220	0.0015823	0.0048041
240	0.0016723	0.0049294

The velocities and temperatures listed are the inlet velocities and temperatures of the homogenous fluid stream entering the die insert.

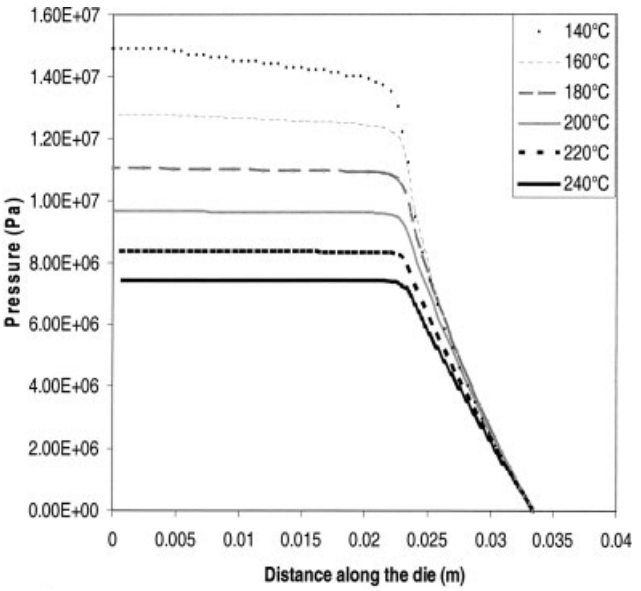

Figure 8 Pressure profiles along the die for different inlet PS-CO_2 solution temperatures (10 rpm screw rotation rate).

the pressure contours were found to become flat after a small entrance length in the capillary die implying that variation in pressure in the radial direction is negligible for all processing conditions studies. The pressure drop profiles along the die for the high flow rates (corresponding to 30-rpm screw rotation rate) for all the different inlet temperatures studied are qualitatively similar to the ones at low flow rates and so are not discussed separately.

The nonlinearity of the pressure drop profiles in the capillary could be attributed to a number of factors, particularly, nonisothermal nature of the flow due to viscous dissipation, viscosity dependence of the PS-CO_2 mixture on pressure and temperature, and hydrodynamic entrance effects. An important implication of the pressure dropping more steeply in the entrance region of the capillary would be that the saturation surface is shifted towards the die entrance, when compared with the case in which a linear pressure profile along the entire length of the capillary is presumed. Consequently, a larger time would be available for the nucleation and bubble growth processes to occur inside the capillary die when compared with the linear pressure drop case. Simultaneously, a reduction in the absolute magnitude of the slope of the pressure profile at the saturation surface would result in a reduced rate of nucleation.

The axial profiles of temperature and velocity for a representative flow condition of 180°C solution temperature at inlet, 1.0 wt % CO_2 concentration, and 10-rpm screw rotation rate are shown in Figure 9. On examining the axial temperature profiles, corresponding to different radial sections in the foaming die [Fig. 9(a)], we find that most of the temperature rise is concentrated in a region very close to the wall. The temperature rise (~ 15°C) is pretty significant and for the highest flow rates studied, the maximum temperature rise could be as much as ~ 24°C. The heated polymer has a lower viscosity and this exaggerates the concentration of shearing near the wall. This tends to localize the viscous heating near the wall, and since the low thermal conductivity limits the rate of heat transfer out of the high-shear-rate region, it can lead to unexpectedly large local temperature rises like the ones we observe.[86] The role of the limited thermal conduction of heat in the melt can also be clearly observed in Figure 9(a). The greatest temperature rise for the adiabatic die is observed at the wall (~ 15°C), while at the centerline the rise in temperature is merely ~ 1°C. The most rapid temperature rise with respect to axial distance occurs in the entrance region of the capillary near the wall and can be attributed to the higher values of the pressure-dependent viscosity and the high shear rates prevailing in this region. The temperature rise per unit axial length decreases with increasing axial distances along the die as can be inferred from the concave-downward nature of the curves for the region near the wall [$r/R > \sim 0.72$ in Fig. 9(a)]. This can be attributed to the monotonically decreasing pressure-dependent shear viscosity as also to the enhanced thermal conduction due to higher radial temperature gradients with increasing axial distances

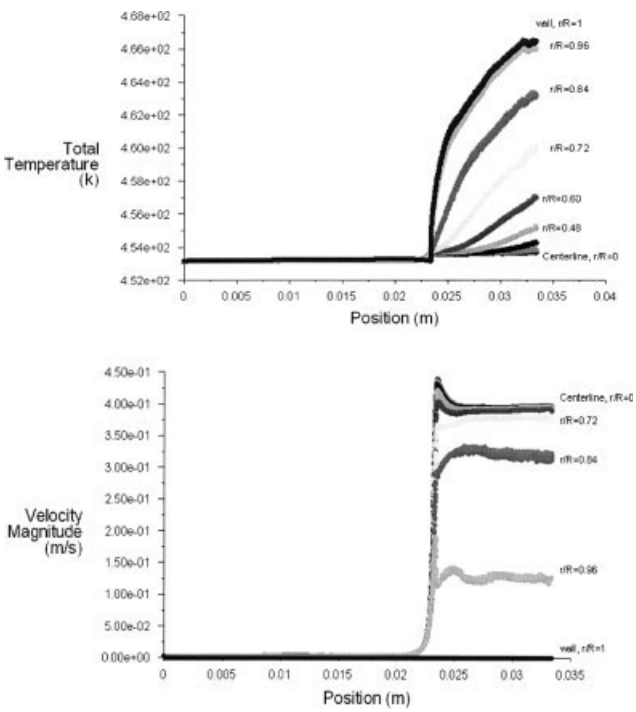

Figure 9 (a) Top: Temperature profiles along the die length (180°C, 1.0 wt % CO_2, 10 rpm screw rotation rate) (b) Bottom: Velocity profiles along the die length (180°C, 1.0 wt % CO_2, 10 rpm screw rotation rate).

along the die. On the other hand, the temperature rise per unit axial length increases with increasing axial distances along the core of the capillary die [$r/R < \sim 0.72$ in Fig. 9(a)] as evident from the concave-upward nature of the curves. This is due to the enhanced thermal conduction with increasing distance from the entrance of the die.

The axial velocity profiles corresponding to different radial sections in the foaming die are shown in Figure 9(b). For an entrance velocity of 0.00135 m/s of the fluid into the guiding hollow tube, the maximum velocity observed in the capillary die is 0.438 m/s, which corresponds to an increase of $\sim$ 325 times. Also, as can be observed from Figure 9(b), right at the entrance of the capillary die, a hump is observed in the velocity magnitude along the core of the flow ($r/R < \sim 0.72$). This hump could possibly be attributed to the redistribution of the velocity components just downstream of the contraction. There is a significant radial component of the velocity as the fluid enters the contraction and the hump, very possibly, represents that region of the die in which radial flow is important enough to contribute significantly to the net velocity magnitude of the fluid flowing through the die. Velocity redistribution takes place within the small capillary die once the fluid has passed through the abrupt contraction. At $L/D \sim 10$, the velocity profile in the die assumes a fixed flattened shape characteristic of shear-thinning polymer melts and hardly changes for greater axial distances along the capillary die.

A comparison between experimental and simulated pressure drops is depicted in Figure 10. It can be seen from Figure 10(a) that at the lower flow rates through the die (corresponding to 10 rpm screw rotation rate), fairly good agreement is obtained between simulated and experimental pressure drops at the higher temperatures (>180°C) studied, but the simulations under predict the pressure drops somewhat at lower temperatures. Figure 10(b) shows that a similar trend is observed for the higher flow rates (corresponding to 30 rpm screw rotation rate) through the die too. Additionally, on comparing Figure 10(a) and Figure 10(b), it appears that the agreement between the experimentally and computationally predicted pressure drops is better for the lower flow rates studied.

A primary reason behind why simulation results under predict somewhat the total pressure drop over the die at the lowest inlet melt temperature or the highest flow rate studied could be the noninclusion of extensional effects in the simulation. As pointed out earlier by Han et al.,[8,22] what a pressure transducer measures when flush-mounted on a capillary is not just the hydrostatic pressure, p, but in fact the outward-acting total wall normal stress, $S_{rr}(R,x)$, which is defined as

$$S_{rr}(R,x) = -p(R,x) + \tau_{rr}(R,x) \quad (22)$$

where $\tau_{rr}(R,x)$ is the extra stress, which is generated due to the deformation of the fluid. The second normal stress coefficient, ψ_2, is negative for concentrated polymer solutions and is generally less than 20% of the magnitude of the first normal stress coefficient, ψ_1, and so does not play as dominant a role as ψ_1 does in dictating fluid rheology.[55] Bird et al.[87] have noted that ψ_1 is positive for most polymers and has a large power law region in which it could decrease by as much as a factor of 10^6. Furthermore, the authors have pointed out that for most polymer systems, the rate of decline of ψ_1 with increasing shear rate is greater than that of η with increasing shear rate. This could help explain why the agreement between simulated and experimentally measured pressure drops appears slightly better at lower flow rates when compared with the higher flow rates studied.

Vinogradov and Malkin[88] have discussed the temperature dependence of normal stresses and have

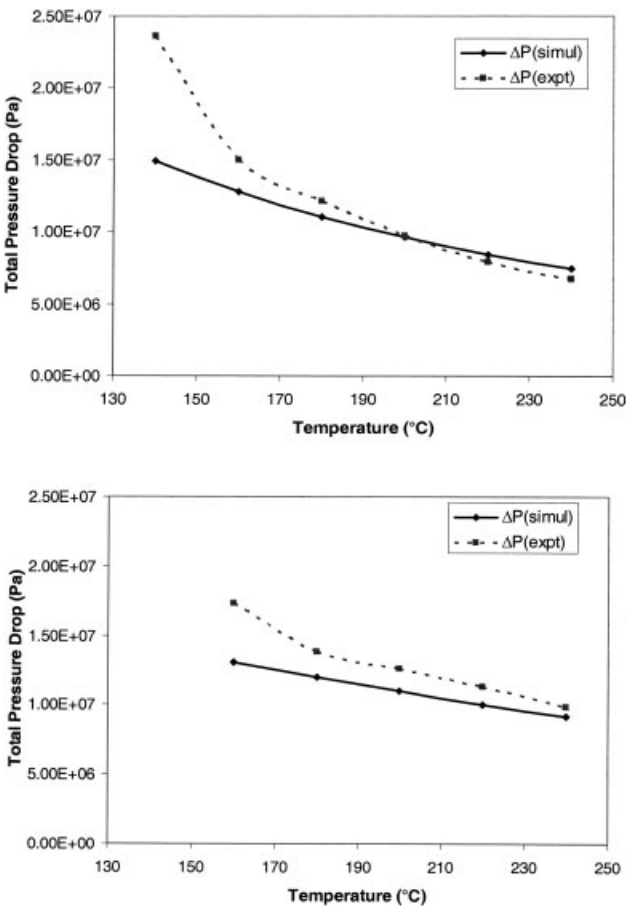

Figure 10 (a) Top: Comparison of Simulated and Experimental Pressure Drops across the die for different inlet PS-CO_2 solution temperatures (10 rpm screw rotation rate) (b) Bottom: Comparison of simulated and experimental pressure drops across the die for different inlet PS-CO_2 solution temperatures (30 rpm screw rotation rate).

concluded that the temperature dependence of the first normal stress coefficient ψ_1 must be stronger than the temperature dependence of the viscosity η. This would imply that at lower temperatures, the extensional effects would begin playing an increasingly dominant role in the rheology of the fluid when compared with their effect at higher temperatures and this could help explain the observation that the experimental and simulated pressure drop rates differ more at lower temperatures than they do at higher temperatures.

Other reasons that could possibly contribute to the slight under prediction of simulated pressure drops from experimental measurements could be the absence of an interaction term in the Chow model to estimate T_g depression for the PS-CO_2 mixture. Simulating the flow under adiabatic conditions while the experiments were conducted for a nearly isothermal die block could also contribute to a small extent in the difference observed between experimental measurements and simulated results. Real flow situations would neither be perfectly adiabatic, nor would they be perfectly isothermal, but would probably resemble an intermediate regime between these two situations.[89]

It must be pointed out that Xue and Tzoganakis[90] have measured the entrance pressure losses for PS-CO_2 solutions as a function of CO_2 concentration (0–4 wt % CO_2 in PS), upstream pressure (20–35 MPa), and wall shear stress (0.04–0.1 MPa). They have shown that dissolution of CO_2 into the PS melt reduces the entrance pressure drop for a given upstream (or entrance) pressure, and that for the conditions that they tested, the extra pressure losses account for only about 5% of the total pressure drops encountered for the solution on flowing through the dies. However, their measurements have only been performed for temperatures above 200°C, where extensional effects are not as significant.

Location of saturation surface

The CO_2 solubilities for the pressure and temperature fields in the die were computed using a separate program incorporating the Sanchez Lacombe Equation of State (SLEOS). The chemical potential of the gas in the mixture is computed using the relation:

$$\begin{aligned}\mu_1 = RT\{&\ln\ \varphi_1 + (1 - r_1/r_2)\varphi_2 \\ &+ r_1^0\tilde{\rho}(P_1^*P_2 - 2P_{12}^*)/(P_1^*T_1)\phi_2^2\} \\ &+ r_1^0RT\{-\tilde{\rho}/\tilde{T}_1 + \tilde{P}_1/(\tilde{\rho}\tilde{T}_1) + (1/\tilde{\rho} - 1)\ln(1 - \tilde{\rho}) \\ &+ (1/r_1^0)\ln\ \tilde{\rho}\} \qquad (23)\end{aligned}$$

where μ_1 is the chemical potential of component 1 (gas) in the binary mixture, R is the gas constant, and the other terms arise from the mixing rules discussed earlier.

The equilibrium solubility of the PS-CO_2 mixture was computed by equating the chemical potential of CO_2 in the liquid and vapor phases and this information was used to determine the location of the saturation curves under the process conditions chosen. Tsujimura et al.[32] estimated the critical pressure for bubble inflation in foam extrusion for the polypropylene–isobutane system and their calculations revealed that the critical pressure was about 0.2–0.4 MPa lower than the equilibrium (saturation) pressure for the mixture. In the discussion that follows, as a first approximation, the terms ''surface of incipient nucleation'' and ''position of nucleation onset'' have been used interchangeably to denote that position along the foaming die, when the polymer solution first becomes supersaturated in its passage through the die, (which is, in principle, different from the position corresponding to the critical pressure for bubble inflation, which is typically used to denote the formation of the second phase in nucleation literature). As shown in Figure 11(a), the position of nucleation onset was located between 27.5 and 30 mm for the different process conditions chosen. Since a large part of the pressure drop occurs in the entrance region of the capillary, the surface of incipient nucleation is located around the middle of the capillary instead of near the exit. Several observations can be made from Figure 11(b–d) about the location of the surface of incipient nucleation in the adiabatic foaming die.

A rise in inlet melt temperature shifts the surface of incipient nucleation towards the entrance of the capillary. For low flow rates (corresponding to 10 rpm screw rotation rate), it appears that the shift is more sensitive to temperature at the lower temperatures used. However, no such sensitivity dependence is apparent at the higher flow rates used. It can be seen from Figure 11(d) that the location of the surface of incipient nucleation is very sensitive to the flow rate (screw rotation rate) at higher temperatures, but the sensitivity diminishes rapidly at lower temperatures. Thus, for example, a rise in the screw rotation rate from 10 to 30 rpm shifts the incipient nucleation surface by $\sim$ 0.75 mm at 240°C while a similar rise in screw rotation rate hardly affects the position of nucleation onset at 180°C.

For all process conditions studied, nucleation appears to occur first at the wall and then at the centerline. This observation appears to be in contrast with the handful of visual observations of bubble nucleation made by researches on extrusion dies[17,22] and possible reasons for this discrepancy are discussed below in detail. For our capillary die, the earlier onset of nucleation at the wall (than at the centerline) can be attributed to the reduced solubility at the higher temperature due to viscous heat generation near the wall. Also, on comparing Figures 11(a) and 11(b), it can be clearly observed that the curvature of

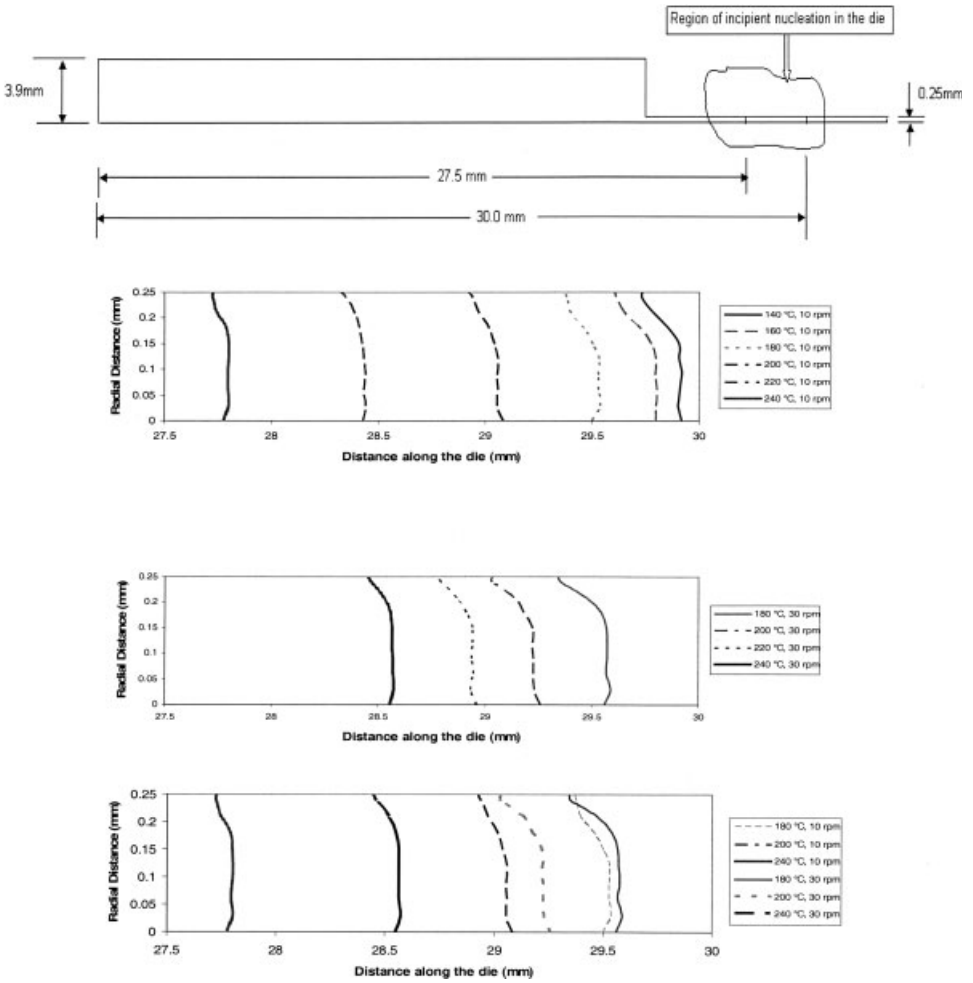

Figure 11 (a) Top: Location of saturation surface in the die. (b) Top middle: Saturation surface curves, 10 rpm. (c) Bottom middle: Saturation surface curves, 30 rpm. (d) Bottom: Effect of screw rotation rate on the location of the saturation surface.

the surface of incipient nucleation is more pronounced at the higher flow rates than at the lower flow rates. This is as expected since the viscous dissipation (and hence the temperature rise) is greater at higher flow rates.

The effect of shear on bubble nucleation in polymer–gas systems is still not completely understood. Han and Han[22] investigated the phenomenon of bubble nucleation in a slit die for the PS-trichlorofluoromethane system. A He–Ne laser was used to illuminate the PS-gas mixture and visual observations of the nucleating and growing bubbles could be made through the provision of an optically clear glass window. The authors observed that the bubbles nucleated first at the center of the slit die ($y = 0$ position) for the PS-trichlorofluoromethane system. Furthermore, the position of nucleation onset was found to shift towards the die exit on moving away from the slit axis in the cross-channel (y) direction but then began shifting again towards the die entrance beyond a certain critical value of y ($y = y_{nc}$). To explain their observations, the authors suggested that bubble nucleation at positions between $y = 0$ and $y = y_{nc}$ was induced by flow and bubble nucleation at positions between $y = y_{nc}$ and $y = h$ (die wall) was induced by shear stress. The authors also noted that cavitation brought about by the surface roughness of the wall and by thermal fluctuations due to the heat transfer between the die wall and the polymer solution could induce nucleation earlier near the wall, but such events would be sporadic and could be ignored so that shear effects would be the dominant mechanism for triggering nucleation earlier near the die wall. Our results lend support to the interpretations of Han and Han[22] for the observed trend in the position of nucleation onset between $y = y_{nc}$ and $y = h$ and demonstrate how shear stress through viscous heat generation at the wall can bend the surface of incipient nucleation towards the die entrance and induce nucleation first near the wall. However, further analysis is required to explain the experimentally observed trend in the position of nucleation onset between the cross-channel positions $y = 0$ and $y = y_{nc}$.

Another very interesting observation that Han and Han[22] made was that while supersaturation seems to be a necessary condition in a homogeneous isotropic system for bubble nucleation to occur under static conditions, for a flowing polymer–gas mixture, bubble nucleation could occur even in an unsaturated condition. It is now well known that the orientation of polymer chains changes in a flow field, with the long polymer chains aligning themselves in the direction of the flow so that they assume a distinctly distinguishable (though difficult to quantify) configuration under flow from their configuration at rest. Han and Han used the Flory Huggins theory to compute their equilibrium solubility curve, which, as noted earlier, does not account for the vacant lattice sites. It will be of interest to compare the experimental results of Han and Han with the equilibrium solubility values for the PS-trichlorofluoromethane system obtained through the SLEOS.

Recently, researchers from the Industrial Materials Institute, NRC, Canada,[31,33,91] used an inline detection method based on ultrasonic sensors to investigate the influence of the flow on the foaming behavior of various PS-gas mixtures in an extrusion slit die. The authors observed that under flow conditions, the degassing pressure was consistently higher than the solubility pressure. A tentative explanation was offered by Tatibouet and Gendron[31] to account for their experimental observations. The authors suggested that the extensional stresses do not have sufficient time to relax at low processing temperatures or for polymers with low values of melt flow index or with large values of compliance and this could lead to premature degassing of the PS-PFA mixture along the die length. Additionally, the authors have quoted the observation of Kim and Dealy[92] that the amount of stretching is at its maximum along the centerline, and have speculated based on this observation that the influence of tensile deformation on degassing could help explain the observation of Han and Han that bubbles nucleate first along the axis in their slit die. Kim and Dealy,[92] in their work, do not appear to have made the observation of stretching being a maximum along the centerline explicitly, but do quote Ramamurthy and McAdam[93] as having demonstrated that the velocity on the center streamline has a large maximum just before the die entry and then falls further downstream, which implies that there is a strong stretching along the centerline and appears to validate the premise of Tatibouet and Gendron.[31] Although Tatibouet and Gendron[31] have suggested a probable cause for the bubbles nucleating first along the centerline of the slit die of Han and Han,[22] considerable work still needs to be done in this area to understand the process within a combined framework of rheology and thermodynamics.

Effect of field gradients on foam morphology

Nucleation events depend on the pressure and temperature history of a fluid element in the foaming die. In this section, the foam morphology is related to the basic field variables—temperature, pressure, and shear rate in the foaming die.

Park et al.[27] have demonstrated the importance of the pressure drop rate on the nucleation density of the polymer foam. Their results have been verified by the experimental work of Han et al.[24] in our laboratory. The pressure drop rate and the temperature rise rate directly affect the solubility drop rate, thereby influencing the foam morphology. The pressure does not change much in the radial direction in the region of nucleation onset in the die. Thus, dP/dx hardly changes across the die cross-section in the region of the die where the pressure in the capillary falls below the degassing pressure of the PS-CO_2 solution. The velocity is predominantly unidirectional in the region of nucleation onset in the capillary and the pressure drop rate can be simply computed as

$$\frac{dP}{dt} = \frac{dP}{dx} v_x \tag{24}$$

where v_x is the local axial velocity. The pressure drop rate along the surface of incipient nucleation for the different conditions studied is presented in Figure 12. Note that the pressure drop rate profile has exactly the same shape as the velocity profile along the surface of incipient nucleation since dP/dx is constant.

Han et al.[24] had observed earlier that while operating at the lowest temperature (140°C) of their processing window, the cell morphology was found to change appreciably from the one observed at higher temperatures—in that larger, conjugated, polyhedral cells were observed under this condition. Their observation is reproduced as Figure 13 here. The authors attributed this change in foam morphology to the increased viscosity and rigidity of the polymer matrix at the lower processing temperature and to the accelerated vitrification of the foam on exiting the extrusion die. Our simulation results indicate that the pressure drop rate is significantly lower for the 140°C case than for any other temperature studied (Fig. 12), which, following Park et al.'s[27] argument, implies that a lesser number of bubbles are able to nucleate under the given conditions, which can eventually grow to larger sizes and impinge on each other forming the polyhedral, conjugated morphology observed by Han et al.[24]

SEM micrographs of foam cross-sections obtained at two different processing rates (corresponding to 10 and 30 rpm screw rotation rate) for 180°C inlet melt

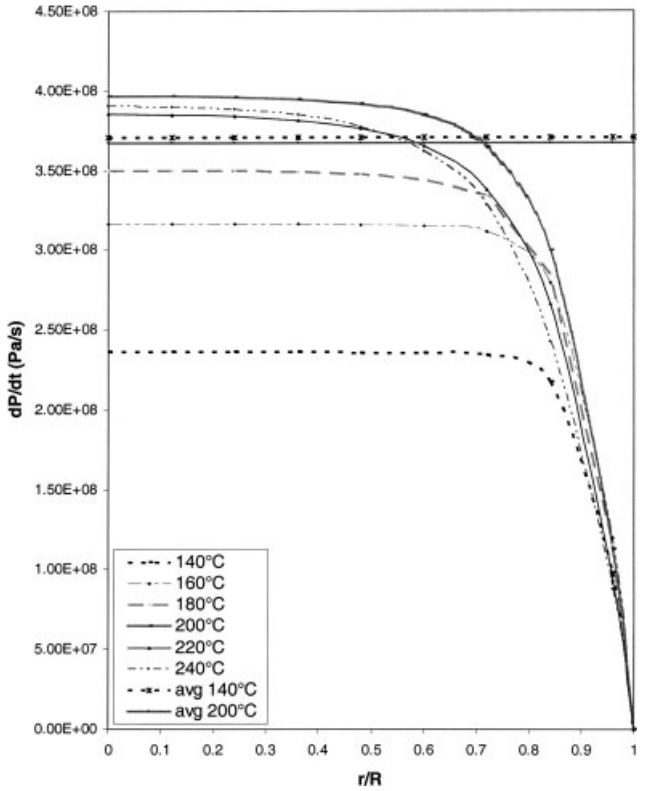

Figure 12 Pressure drop rate at different temperatures (10 rpm screw rotation rate) at the saturation surface. The straight lines are pressure drop rates computed for an average velocity and a linear pressure drop profile along the die length. Note that because of the very steep pressure drop near the entrance of the capillary die for the 140°C case, the pressure drop rate predicted from an average velocity and a linear pressure drop is far higher than the true pressure drop rate at the surface of incipient nucleation.

temperature and 1.0 wt % CO_2 are shown in Figure 14. Cell density was calculated at four different radial locations for each SEM micrograph, using the following well-known expression.[13]

$$N_f = \left(\frac{nM^2}{A}\right)^{3/2} \tag{25}$$

where N_f is the number of bubbles per centimeter cube of the final foam, n is the number of bubbles in the micrograph, A is the area of the micrograph, cm^2, and M is the magnification factor of the micrograph.

The cell density (expressed as no. of cells/cm^3) is plotted against radial position (expressed as r/R) in Figure 14. For each throughput rate used, cell density was found to decrease by almost an order of magnitude in going from the center to the edge of the foam section. Also, for the same r/R, the cell density in the foam sample corresponding to the higher throughput rate was found to be higher by almost an order of magnitude when compared with the cell density in the foam sample corresponding to the lower throughput rate. These observations substantiate the observations of Park et al.[27] and Han et al.[24] regarding the importance of the pressure drop rate in determining bubble nucleation density.

However, the morphology of our foam samples differs from the foam morphologies obtained by Chen et al.[18] and Xu et al.[34] in one essential respect—in that they observed an increase in cell density (and a corresponding decrease in cell size) near the edge of their foam samples while we observed fewer and larger cells near the edge of all our foam samples. Complete details regarding how the process parameters were controlled for their foaming experiments are not available, and hence it is not clear what the abovementioned differences in cell morphologies might be attributed to.

Thermal gradients across adjacent mesh volumes are appreciable in the capillary die due to significant viscous heat dissipation. The temperature rise rate dT/dt of a given fluid element in the die is calculated based on the following procedure. The axial tempera-

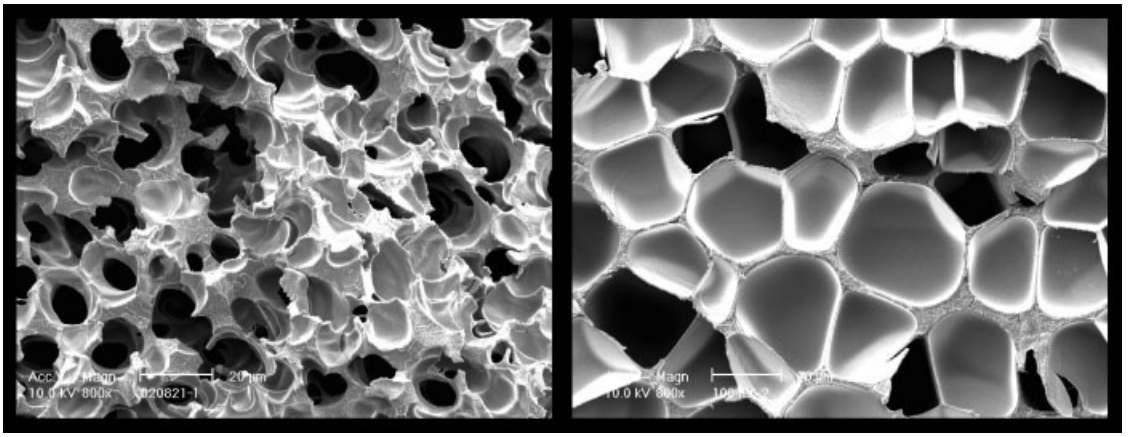

Figure 13 SEM micrographs depicting cell morphology at 160°C, 10 rpm (left) and 140°C, 10 rpm (right). Note the much larger, noncoalescing cell morphology at 140°C (right) compared with the smaller, coalescing cell morphology at 160°C (left).

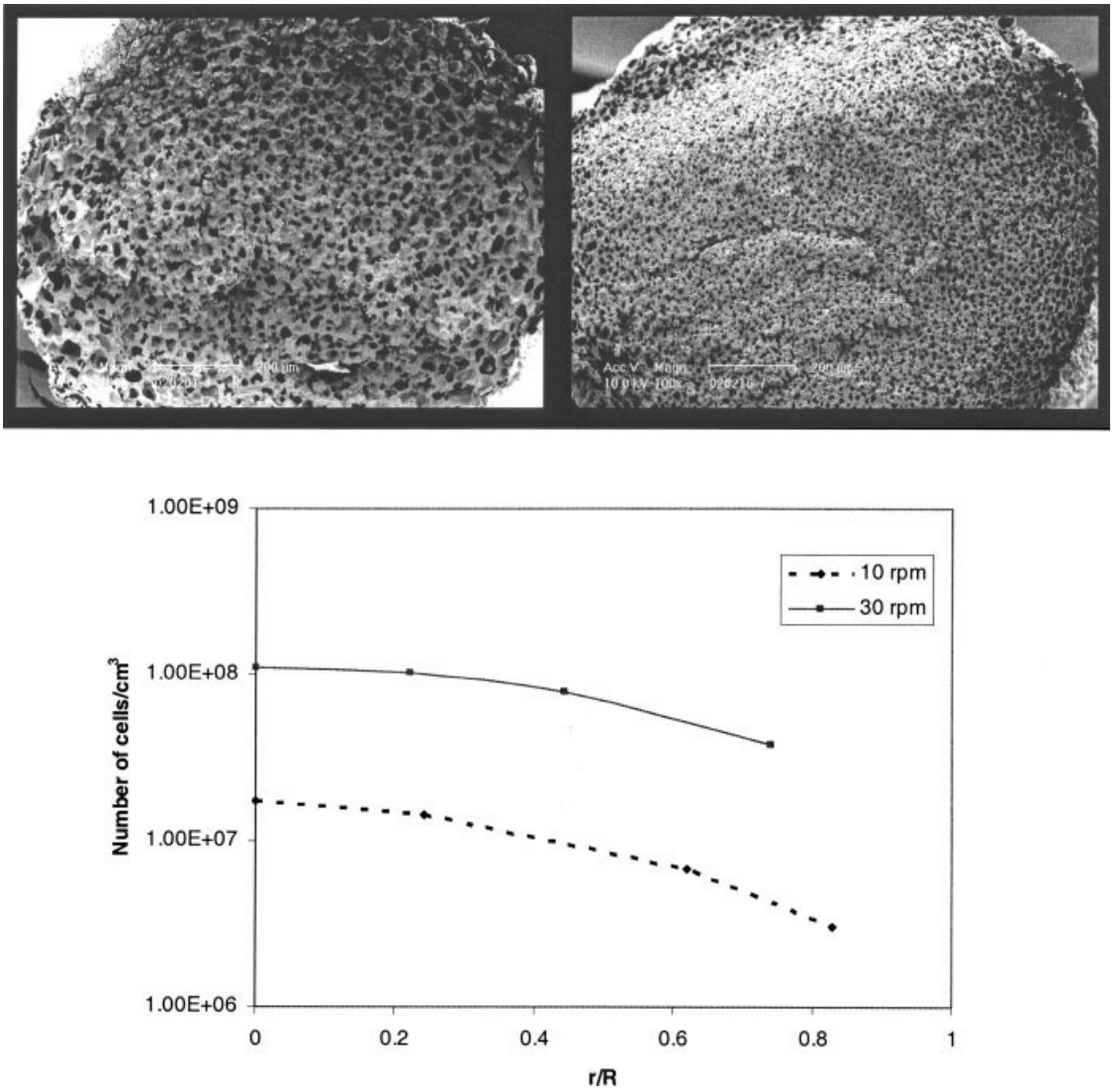

Figure 14 (a) Top: Cell morphology (180°C). The figures at the left and right represent the morphology at the lower processing rate (corresponding to 10 rpm screw rotation rate) and higher processing rate (corresponding to 30 rpm screw rotation rate) respectively. (b) Bottom: Cross-sectional cell density distribution for the micrograph corresponding to Figure 14(a). There is a significant decrease in cell density as one goes from the center to the edge of each SEM micrograph in Figure 14(a). Also, there is about an order of magnitude increase in cell density for corresponding positions of the cell morphology for the higher processing rate micrograph (30 rpm) when compared with the lower processing rate micrograph (10 rpm).

ture distribution along a specified radial distance in the capillary is approximated using a polynomial expression of appropriate degree. The axial temperature gradient at the surface of incipient nucleation is then computed by taking the derivative of the polynomial expression at the point of interest. The temperature rise rate along the die can now be calculated using an expression equivalent to eq. (24), i.e.,

$$\frac{dT}{dt} = \frac{dT}{dx} v_x \tag{26}$$

Figure 15 represents the temperature rise rate along the surface of incipient nucleation for the different conditions studied. The temperature rise rate peaks at around four-fifth of the radial distance from the center, as can be seen from Figure 15. Unlike the pressure drop rate, the temperature rise rate does not seem to have a significant effect on the cell size distribution under the prevailing flow conditions.

Although proper viscoelastic scaling of the shear viscosity can predict pressure drops in semiquantitative agreement with experimental measurements, care must be taken while implementing the methodology to predict the pressure drop across the die at lower processing temps where normal stresses become important. West[94] has observed that for different polydisperse PS samples that he measured, the

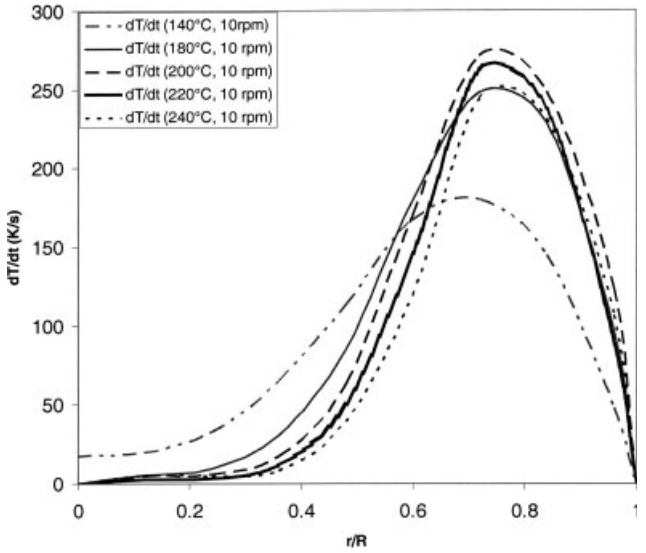

Figure 15 Dependence of temperature rise rate on inlet melt temperature (10 rpm screw rotation rate) at the saturation surface. Notice that for the slower moving melt (140°C) there is greater time available for the viscous heat generated to diffuse inwards and thus the 140°C curve has a broader radial spread than the others.

maximum relaxation times at 227°C ranged from 0.011 to 0.488 s. Such long relaxation times are comparable to the mean residence time of the fluid elements in the die implying that there could be a significant extensional component of the flow. The bubble nucleation and growth processes downstream of the surface of saturation are also complicated by the fact that these processes are occurring in a regime wherein the polymer chains are undergoing complex transitional rearrangements to their equilibrium configuration and where extensional effects through elastic recoil may play as important a role as shear effects. Given the complexity of the foaming process in the extrusion foaming of thermoplastics, a very careful analysis of experimental data is essential to sort out the effect of the different processing parameters and process conditions on bubble nucleation and growth.

CONCLUSIONS

An internally consistent viscoelastic scaling approach has been developed to scale up the shear viscosity of the fluid that accounts for the temperature, pressure as well as concentration dependence of the shear viscosity in a dynamic way along each cell element in the mesh of the foaming die. The pressure drop values predicted by the simulations give good qualitative (and even semiquantitative) agreement with experimentally obtained pressure drop values under nearly identical flow conditions.

Simulations have been performed for the flow of a polymer-diluent solution through an abrupt axisymmetric contraction extrusion foaming die. The axial profiles of the basic field variables: pressure, temperature, and velocity are obtained for different radial sections of the capillary die. From knowledge of the pressure and temperature fields and using the SLEOS, the location of the saturation curves (also referred to as ''the surface of incipient nucleation'' in this work) in the foaming die are estimated. The shape of the surface of nucleation onset is compared with the handful of experimental data that have been reported in the literature and differences between the computed and measured profiles are discussed in detail. Also, the pressure drop rate and the temperature rise rate have been computed across the surface of incipient nucleation and their implications on the final foam morphology have been discussed.

Measurement and subsequent incorporation of normal stress functions and extensional stresses for polymer-blowing agent solutions into the simulation can improve the model predictions. Also, once the time lag of nucleation for PS-CO_2 mixture is evaluated, use of a multiphase model to simulate the flow of the two-phase polymer–gas mixture downstream of the surface of incipient nucleation will enhance the predictions. The next step would be to estimate the rate of bubble nucleation from knowledge of the hydrodynamics and the basic field variables—pressure, temperature and velocity of the PS-CO_2 mixture in the die. Finally, a suitable bubble growth model will be incorporated in the simulation to predict the microstructure of the final foam.

We thank Dr Xiangmin Han for the experimental data and Dr Dehua Liu for help with the SLEOS.

References

1. Spitael, P.; Macosko, C. W.; McClurg, R. B. Macromolecules 2004, 37, 6874.
2. Throne, J. L. Thermoplastic Foam Extrusion: An Introduction; Hanser Publishers: Munich, 2004.
3. Hansen, R. H. SPE J 1962, 18, 77.
4. Han, C. D.; Kim, Y. W.; Malhotra, K. D. J Appl Polym Sci 1976, 20, 1583.
5. Blyler, L. L.; Kwei, T. K. J Polym Sci Part C: Polym Symp 1971, 35, 165.
6. Oyanagi, Y.; White, J. L. J Appl Polym Sci 1979, 23, 1013.
7. Han, C. D.; Villamizar, C. A. Polym Eng Sci 1978, 18, 687.
8. Han, C. D. Multiphase Flow in Polymer Processing; Academic Press: New York, 1984.
9. Arora, K. A.; Lesser, A. J.; McCarthy, T. J. Macromolecules 1998, 31, 4614.
10. Colton, J. S.; Suh, N. P. Polym Eng Sci 1987, 27, 485.
11. Colton, J. S.; Suh, N. P. Polym Eng Sci 1987, 27, 493.
12. Goel, S. K.; Beckman, E. J. AIChE J 1995, 41, 357.
13. Kumar, V.; Suh, N. P. Polym Eng Sci 1990, 30, 1323.
14. Ramesh, N. S.; Rasmussen, D. H.; Campbell, G. A. Polym Eng Sci 1994, 34, 1698.
15. Ramesh, N. S.; Rasmussen, D. H.; Campbell, G. A. Polym Eng Sci 1994, 34, 1685.

16. Rodeheaver, B. A.; Colton, J. S. Polym Eng Sci 2001, 41, 380.
17. Taki, K.; Nakayama, T.; Yatsuzuka, T.; Ohshima, M. J Cell Plast 2003, 39, 155.
18. Chen, L.; Wang, X.; Straff, R.; Blizard, K. Polym Eng Sci 2002, 42, 1151.
19. Gendron, R.; Huneault, M.; Tatibouet, J.; Vachon, C. Cell Polym 2002, 21, 315.
20. Han, C. D.; Ma, C. J Appl Polym Sci 1983, 28, 831.
21. Han, C. D.; Ma, C. J Appl Polym Sci 1983, 851.
22. Han, J. H.; Han, C. D. Polym Eng Sci 1988, 28, 1616.
23. Han, X.; Koelling, K. W.; Tomasko, D. L.; Lee, L. J. Polym Eng Sci 2002, 42, 2094.
24. Han, X.; Koelling, K. W.; Tomasko, D. L.; Lee, L. J. Polym Eng Sci 2003, 43, 1206.
25. Lee, S. T. Foam Extrusion: Principles and Practice; Technomic: Lancaster, PA, 2000.
26. Naguib, H. E.; Park, C. B.; Reichelt, N. J Appl Polym Sci 2004, 91, 2661.
27. Park, C. B.; Baldwin, D. F.; Suh, N. P. Polym Eng Sci 1995, 35, 432.
28. Park, C. B.; Behravesh, A. H.; Venter, R. D. Polym Eng Sci 1998, 38, 1812.
29. Park, C. B.; Suh, N. P. Polym Eng Sci 1996, 36, 34.
30. Shimoda, M.; Tsujimura, M.; Ohshima, M. J Cell Plast 2001, 37, 517.
31. Tatibouet, J.; Gendron, R. J Cell Plast 2004, 40, 27.
32. Tsujimura, I.; Toru, M.; Mamoru, I.; Hirokatsu, M. Seikei-Kakou 2002, 14, 185.
33. Vachon, C.; Gendron, R. Cell Polym 2003, 22, 75.
34. Xu, X.; Park, C. B.; Xu, D.; Pop-Iliev, R. Polym Eng Sci 2003, 43, 1378.
35. Tomasko, D. L.; Li, H.; Liu, D.; Han, X.; Wingert, M.; Lee, L. J.; Koelling, K. W. Ind Eng Chem Res 2003, 42, 6431.
36. Xu, X.; Park, C. B. Ind Eng Chem Res, submitted.
37. Colton, J. S.; Suh, N. P. Polym Eng Sci 1990, 27, 485.
38. Areerat, S.; Nagata, T.; Ohshima, M. Polym Eng Sci 2002, 42, 2234.
39. Bae, Y. C.; Gulari, E. J Appl Polym Sci 1998, 63, 459.
40. Gerhardt, L. J.; Garg, A.; Manke, C. W.; Gulari, E. J Polym Sci Part B: Polym Phys 1998, 36, 1911.
41. Gerhardt, L. J.; Manke, C. W.; Gulari, E. J Polym Sci Part B: Polym Phys 1997, 35, 523.
42. Kwag, C.; Manke, C. W.; Gulari, E. J Polym Sci Part B: Polym Phys 1999, 37, 2771.
43. Kwag, C.; Manke, C. W.; Gulari, E.; Ind Eng Chem Res 2001, 40, 3048.
44. Lee, M.; Park, C. B.; Tzoganakis, C. Polym Eng Sci 1999, 39, 99.
45. Royer, J. R.; DeSimone, J. M.; Khan, S. A. J Polym Sci Part B: Polym Phys 2001, 39, 3055.
46. Royer, J. R.; Gay, Y. J.; Desimone, J. M.; Khan, S. A. J Polym Sci Part B: Polym Phys 2000, 38, 3168.
47. Schummer, P.; Worthoff, R. H. Chem Eng Sci 1978, 33, 759.
48. Williams, M. L.; Landel, R. F.; Ferry, J. D. J Am Chem Soc 1955, 77, 3701.
49. Rohn, C. L. Analytical Polymer Rheology: Structure-Processing-Property Relationships; 1995.
50. Lomellini, P. Polymer 1992, 33, 4983.
51. Mendelson, R. A. Polym Eng Sci 1976, 16, 690.
52. Guaita, M.; Chiantore, O.; Costa, L. Polym Degrad Stab 1985, 12, 315.
53. Clay, J. D. Chemical Engineering Department; The Ohio State University: Columbus, OH, 1997.
54. Ferry, J. D. Viscoelastic Properties of Polymers, 3rd ed.; Wiley: New York, 1980.
55. Tanner, R. I. Engineering Rheology, 2nd ed.; Oxford University Press: New York, 2000.
56. Condo, P. D.; Sanchez, I. C.; Panayiotou, C. G.; Johnston, K. P. Macromolecules 1992, 25, 6119.
57. Chow, T. S. Macromolecules 1980, 13, 362.
58. Hill, T. L. An Introduction to Statistical Thermodynamics; Addison-Wesley: Reading, MA, 1960; p 247.
59. Chiou, J. S.; Barlow, J. W.; Paul, D. R. J Appl Polym Sci 1985, 30, 2633.
60. Kadijk, S. E.; vandenBrule, B. H. A. A. Polym Eng Sci 1994, 34, 1535.
61. Liang, J. Z. Polymer 2001, 42, 3709.
62. Penwell, R. C.; Porter, R. S. J Appl Polym Sci 1969, 13, 2427.
63. Penwell, R. C.; Porter, R. S. J Polym Sci Part A-2: Polym Phys 1971, 9, 463.
64. Penwell, R. C.; Porter, R. S.; Middleman, S. J Polym Sci A-2: Polym Phys 1971, 9, 731.
65. Schouten, J. A.; Scholten, J.; Nelissen, L.; Nies, E. Polym Commun, 1991, 32, 421.
66. Quach, A.; Simha, R. J Appl Phys 1971, 42, 4592.
67. Hieber, C. A.; Chiang, H. H. Rheol Acta 1989, 28, 321.
68. Cross, M. M. Eur Polym J 1966, 2, 299.
69. Vinogradov, G. V.; Malkin, A. Y. J Polym Sci Part A: Gen Pap 1964, 2, 2357.
70. Vinogradov, G. V.; Malkin, A. Y. J Polym Sci Part A-2: Polym Phys 1966, 4, 135.
71. Rouse, P. E. J Chem Phys 1953, 21, 1272.
72. Takahashi, H.; Matsuoka, T.; Kurauchi, T. J Appl Polym Sci 1985, 30, 4669.
73. Picot, J. J. C.; Goobie, G. I.; Mawhinney, G. S. Polym Eng Sci 1982, 22, 154.
74. Wallace, D. J.; Moreland, C.; Picot, J. J. C. Polym Eng Sci 1985, 25, 70.
75. Venerus, D. C.; Schieber, J. D.; Iddir, H.; Guzman, J. D.; Broerman, A. W. Phys Rev Lett 1999, 82, 366.
76. Sakakibara, Y.; Yamada, I.; Hiraoka, S.; Aragaki, T. J Chem Eng Jpn 1990, 23, 499.
77. Sanchez, I. C.; Lacombe, R. H. Macromolecules 1978, 11, 1145.
78. Sato, Y.; Yurugi, M.; Fujiwara, K.; Takishima, S.; Masuoka, H. Fluid Phase Equilib 1996, 125, 129.
79. Liu, D.; Tomasko, D. L. Personal Communication, 2005.
80. Sanchez, I. C.; Lacombe, R. H. J Phys Chem 1976, 80, 2352.
81. Karasz, F. E.; Bair, H. E.; O'Reilly, J. M. J Phys Chem 1965, 69, 2657.
82. Versteeg, H. A.; Malalasekera, W. An Introduction to Computational Fluid Dynamics: The Finite Volume Method; Longman Scientific &Technical: Essex, England, 1995.
83. McClurg, R. B. Chem Eng Sci 2004, 59, 5779.
84. Shidara, H.; Denn, M. M. J Non-Newtonian Fluid Mech 1993, 48, 101.
85. Rosenbaum, E. E.; Hatzikiriakos, S. G. AIChE J 1997, 43, 598.
86. Dinh, S. M.; Armstrong, R. C. AIChE J 1982, 28, 294.
87. Bird, R. B.; Armstrong, R. C.; Hassager, O. Dynamics of Polymeric Liquids, 2nd ed.; John Wiley Sons, 1987; Vol. 1.
88. Vinogradov, G. V.; Malkin, A. Y. Rheology of Polymers; Mir Publishers, 1980.
89. Cox, H. W.; Macosko, C. W. AIChE J 1974, 20, 785.
90. Xue, A.; Tzoganakis, C. J Polym Eng 2003, 23, 1.
91. Sahnoune, A.; Tatibouet, J.; Gendron, R.; Hamel, A.; Piche, L. J Cell Plast 2001, 37, 428.
92. Kim, S.; Dealy, J. M. Polym Eng Sci 2002, 42, 482.
93. Ramamurthy, A. V.; McAdam, J. C. H. J Rheol 1980, 24, 167.
94. West, G. H. Polymer 1969, 10, 751.